Applied Energy 389 (2025) 125761

Contents lists available at ScienceDirect

Applied Energy

journal homepage: www.elsevier.com/locate/apenergy

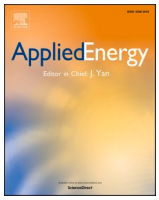

Electromechanical modeling and experimental validation of an origami-structured triboelectric vibration energy harvester

Zicheng Liu [a], Guobiao Hu [b], Yawei Wang [b], Heesoo Yoon [a], Chaoyang Zhao [a], Xin Li [c], Yaowen Yang [a,*]

[a] School of Civil and Environmental Engineering, Nanyang Technological University, 50 Nanyang Avenue, 639798, Singapore
[b] Thrust of Internet of Things, The Hong Kong University of Science and Technology (Guangzhou), Nansha, Guangzhou 511400, China
[c] Advanced Manufacturing Technology Innovation Center, Xidian University, Guangzhou 510555, China

HIGHLIGHTS

- Proposes a model for origami-structured triboelectric energy harvesters (OTEHs).
- Develops a capacitive-based electrical model for non-parallel triangular plates.
- Models and validates OTEHs for vibration energy harvesting with enlarged contact areas.
- Confirms model accuracy in predicting nonlinear dynamics for elastic OTEHs.
- Demonstrates OTEHs' utility by lighting 24 LEDs and powering an IoT sensing node.

ARTICLE INFO

Keywords:
Origami
Electromechanical model
Triboelectric energy harvester
Vibration energy harvesting
Internet of things

ABSTRACT

This study presents a novel electromechanical model and its experimental validation for an origami-structured triboelectric energy harvester (OTEH) designed to scavenge kinetic energy from vibration. OTEHs are recognized for their enhanced electrical output due to increased contact areas from stacked structures, but their electromechanical modeling remains largely unexplored due to geometric complexity. Furthermore, few studies have investigated the use of OTEHs for harvesting vibration energy. To address these gaps, we developed an electromechanical model specifically tailored for vibration energy harvesting using OTEHs. The model integrates an electrical model for triangular non-parallel contact surfaces with a lumped-parameter mechanical model, incorporating origami geometric parameters for broad applicability. We experimentally validated the model using a bellow-origami-structured triboelectric energy harvester (BOTEH) designed for vibration energy harvesting. Benefiting from axial elasticity and a guiding rod, the BOTEH structure can be excited by harmonic base vibration, enabling a systematic investigation of its vibration-energy-harvesting potential. The model, validated through time-domain and frequency-domain voltage and displacement responses under various vibratory conditions, accurately predicts the BOTEH's dynamic behavior. Additionally, under base forcing vibration, the BOTEH demonstrated practical utility by triggering an Internet-of-Things (IoT) temperature sensor and illuminating 24 LEDs, achieving a maximum output power of 119 μW at 6.6 Hz and 0.8 g with an 80 MΩ external resistor.

1. Introduction

The pursuit of harvesting ambient kinetic energy to power small electronics operating at micro- to milliwatt power levels has been a key research focus, driven by the widespread commercialization and application of Internet-of-Things (IoT) node devices [1,2]. The ambient environment is rich with kinetic energy sources—such as wind flow, water waves, human motion, and vehicle dynamics—that often go unutilized. Researchers have devoted significant efforts to developing techniques that efficiently convert ambient vibration energy into electricity, meeting the power requirements of IoT devices. Common energy conversion mechanisms include electromagnetic [3,4], piezoelectric

* Corresponding author.
E-mail address: cywyang@ntu.edu.sg (Y. Yang).

https://doi.org/10.1016/j.apenergy.2025.125761
Received 25 November 2024; Received in revised form 3 March 2025; Accepted 17 March 2025
Available online 27 March 2025

[5,6], electrostatic [7,8], and triboelectric [9,10] transductions. Among these, triboelectric transduction for ambient vibration energy harvesting is relatively new [11] and has gained interest due to its broad material availability, low cost [12], design flexibility [13], and high energy conversion efficiency [14].

Triboelectric energy harvesters (TEHs) generate electricity through triboelectric transduction, which involves the contact between two materials with opposite electron affinities (a tribo-pair) and the electrostatic effect resulting from the induced voltage potential between the oppositely charged materials in relative motion [15]. TEHs operate in four main modes: vertical contact-separation, [16], lateral sliding [17], freestanding [18,19], and single-electrode [20]. In all these modes, larger contact areas between the tribo-pair result in greater triboelectric charge induction and, consequently, higher electrical output. To enhance output, researchers have focused on optimizing structural designs to increase the contact area, including stacking and multilayering tribo-pairs. For example, Yang et al. [21] developed a three-dimensional multilayered TEH in contact-separation mode by stacking tribo-pairs and designed a triple-cantilever-based TEH with stacked tribo-pairs between cantilever beams [10]. Other approaches include tribo-pairs layered inside spring steel plates [22] and zigzag-shaped Kapton films placed inside floating acrylic balls for water wave energy harvesting [23]. While promising, these prototypes can be complex to fabricate and may lack compactness.

Another method to increase the tribo-pair's contact area in a TEH within a limited volume is through the use of origami structures. Origami, the Japanese art of paper folding, involves transforming a two-dimensional (2D) sheet into a three-dimensional (3D) structure. Due to their flexibility, origami structures have found numerous engineering applications, particularly in biomedical fields, [24,25], robotics [26,27], space structures [28,29], and more. Given their engineering appeal, many researchers have incorporated origami structures into TEH designs because paper folding easily creates stacked and multilayered structures, enhancing the contact area between tribo-pairs.

For example, Chung et al. [30] developed a hybrid tribo-piezoelectric energy harvester using a triangulated cylindrical origami structure to achieve a large surface area for the triboelectric component. When compressed vertically, the gaps between the tribo-pairs on the triangulated surfaces close, allowing contact, while piezoelectric patches on the back trigger current flow due to surface deformation. This design permits rotation around the vertical axis during compression, leading to the inclusion of a rotational TEH at the top substrate. However, the fabrication process is complex.

Some origami-based TEHs (OTEHs) utilize simpler structures. For instance, Hu et al. [31] proposed a TEH based on an origami structure requiring only two strips of materials constituting the tribo-pair. One strip is polymer-coated, and the other is a flexible soft conducting strip. These are interlaced and folded to form a TEH capable of producing electrical output from hand-tapping motions. Tao et al. [32] proposed a similar OTEH design utilizing two strips of flexible materials—fluorinated ethylene propylene (FEP) films and copper foils—but with a square rather than octagonal cross-section. This design was applied to practical scenarios, including energy harvesting from human motions and water waves, though it generally lacks sufficient elasticity for vibratory scenarios.

To achieve more elasticity in an origami-structured TEH, Tao et al. [33] proposed a design leveraging the Miura-origami structure's elastic nature. Their TEH (M-TEH) uses two strips of electret forming the tribo-pair, folded and interlaced into a highly elastic Miura structure capable of deforming in multiple directions and returning to its original shape. The structure is flexible enough to be sealed in a tube to prevent humidity from affecting its output. Another example is the bellow-fold origami structured TEH (BOTEH) developed by Chung et al. [34], which combines a fluttering TEH for both vibration and wind flow energy harvesting. The BOTEH, based on a cylindrical origami structure with triangulated surfaces, effectively harvests vibration energy due to its elasticity. Beneath the BOTEH, a fluttering TEH with free polyimide strips and fixed aluminum electrodes harvests energy from wind flow induced by its operation.

In summary, OTEHs are highly flexible and can be designed for various application scenarios, but most research is purely experimental and application-oriented [30,31,33,35]. Comprehensive electromechanical modeling of OTEHs with experimental validation is scarcely found in the literature. Although Hu et al. provided a mathematical proof for the surface enlargement phenomenon [31], comprehensive modeling of OTEHs' electromechanical dynamics is nearly nonexistent due to the complexity of their geometric structures combined with the nonlinear electrical response of TEHs. The diverse and complex application scenarios of OTEHs make it cumbersome to adjust electromechanical parameters of experimental prototypes through trial and error. An electromechanical model would allow for pre-application simulations, reducing the need for experimental modifications.

Additionally, most studies on OTEHs focus on harvesting kinetic energy from press-and-release motions, such as those from human and vehicle movements [33,35], while few have explored their potential for vibration energy harvesting, a ubiquitous kinetic energy source. Current triboelectric vibration energy harvesters typically use a single pair of parallel or non-parallel plates as the substrates for the tribo-pair [36,37] and have limited contact areas. Thus, vibrational TEHs could benefit from the stacked nature of origami structures for enhanced electrical output [31,33]. While Tao et al. experimentally characterized the electrical output of the M-TEH excited by base vibration from water waves [32], its electromechanical modeling remains uninvestigated.

To address these research gaps, this work proposes and experimentally validates a novel electromechanical model of an OTEH with axial elasticity—the first of its kind. Given the unique triangular contact surfaces between tribo-pairs in many OTEHs [30,35], this model introduces a capacitive electrical model for non-parallel triangular contact surfaces. Designed specifically for vibration energy harvesting, the mechanical model, coupled with the electrical model, simplifies the elastic OTEH into a lumped-parameter spring-mass-damper structure. The complete electromechanical model is experimentally validated using a TEH based on the bellow-origami structure that possesses triangular contact surfaces for tribo-pairs [34,35]. The BOTEH is fabricated by folding a plastic sheet with 2D-printed metal electrodes. To effectively harvest vibration energy, the BOTEH is optimized for vertical base excitation using a guiding rod through the proof mass on top. Due to the elasticity of the bellow-fold structure combined with the guiding rod, the BOTEH can produce electrical voltage under forcing vertical base vibration on a seismic shaker. Additionally, the BOTEH's electrical output under forcing base vibration is showcased through experimental characterization and is shown to be sufficient to power real-world IoT devices. The details of this work are presented in the following sections. Section 2 presents the derivation of the electromechanical model of an elastic OTEH for vibration energy harvesting. Section 3 details the structural design, folding procedures, fabrication processes, and the determination of geometric and electromechanical parameters of the BOTEH used for experimental validation of the model. Section 4 explains the experimental setup, results, and relevant discussions, including the experimental validation of the model's predictions for the BOTEH's voltage response in the time and frequency domains under different vibratory conditions, the validation of the equivalent circuit modeling of the theoretical model, and a performance demonstration. Finally, Section 5 summarizes this work.

2. Electromechanical model of an elastic OTEH

2.1. Electrical model

This section details the derivation of the electromechanical model for a generic elastic OTEH in vibration energy harvesting scenarios. Elastic OTEHs often feature triangulated contact surfaces between the tribo-pair, as seen in the design proposed by Chung et al. [30]. An isometric view of a typical pair of such contact surfaces is shown in Fig. 1 (a). These surfaces consist of triangular substrate plates sharing the same base line but capable of separation at an angle. The upper contact surface is bonded with a metal film, while the lower one has a dielectric layer atop a metal film, forming a metal-dielectric interface. The upper and lower metal films are connected to an external resistor R.

The working mechanism of the metal-dielectric interface is illustrated in Fig. 1 (b). During contact-separation cycles, the dielectric layer acquires negative charges, while the upper metal layer gains positive charges due to the triboelectric effect. When the surfaces separate, an air gap forms between the upper metal and lower dielectric layers, causing negative charges to flow from the lower to the upper metal layer to maintain electrostatic equilibrium. Upon recontact, the negative charges transfer back to the lower metal layer, generating an alternating current (AC) voltage across the external resistor, R.

The voltage generation mechanism illustrated in Fig. 1 (a) is explained by the electrical model depicted in Fig. 2. Unlike the non-parallel rectangular capacitive plate model [37–39], this model accounts for triangular contact surfaces, requiring additional integration. Although other OTEHs may have different contact surface shapes, such as the trapezoidal surface proposed by Zhang et al. [35], only minor adjustments to the integration method introduced here would be needed. In Fig. 2, the FEP layer is assumed to have acquired negative charges $-\sigma A_c$, where σ is the surface charge density and A_c is the area of the FEP layer's upper surface. A_c can be expressed as

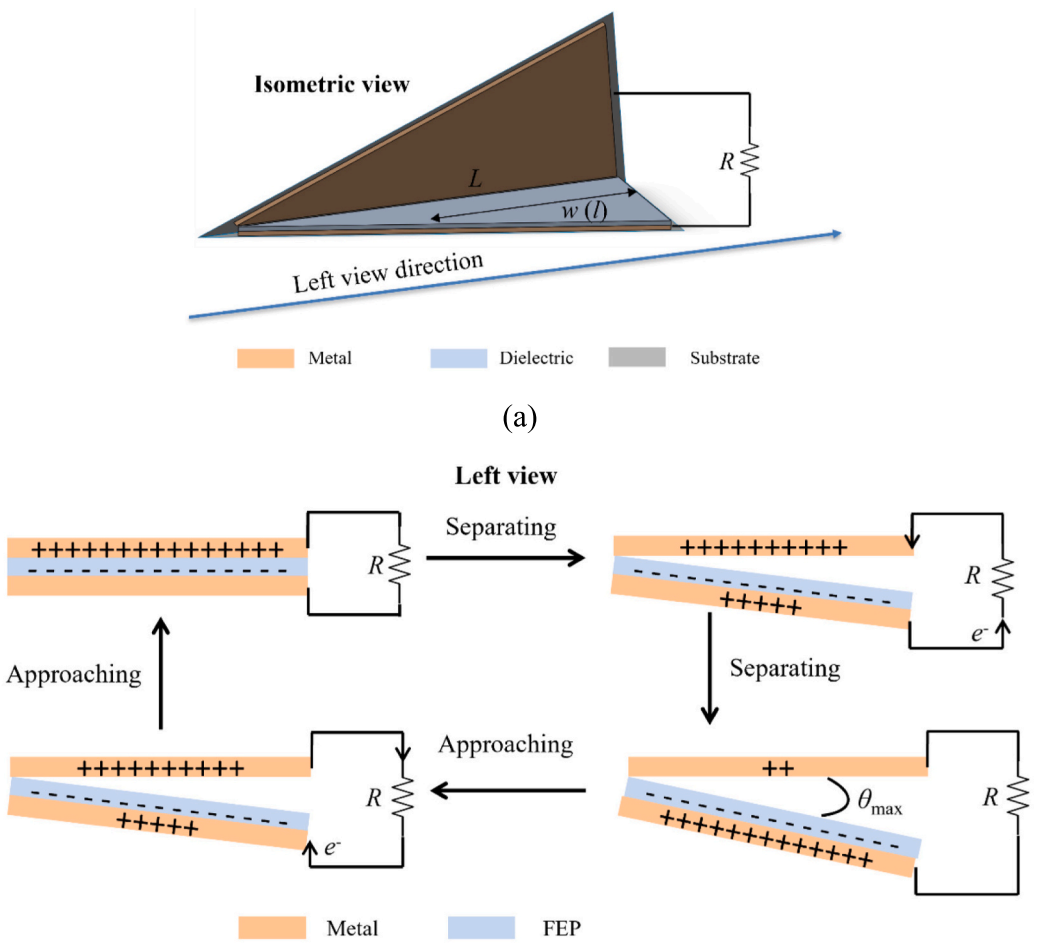

Fig. 1. (a) Isometric view of a typical pair of triangular triboelectric contact surfaces and (b) its electric current generation mechanism through metal-dielectrics interface shown in left view.

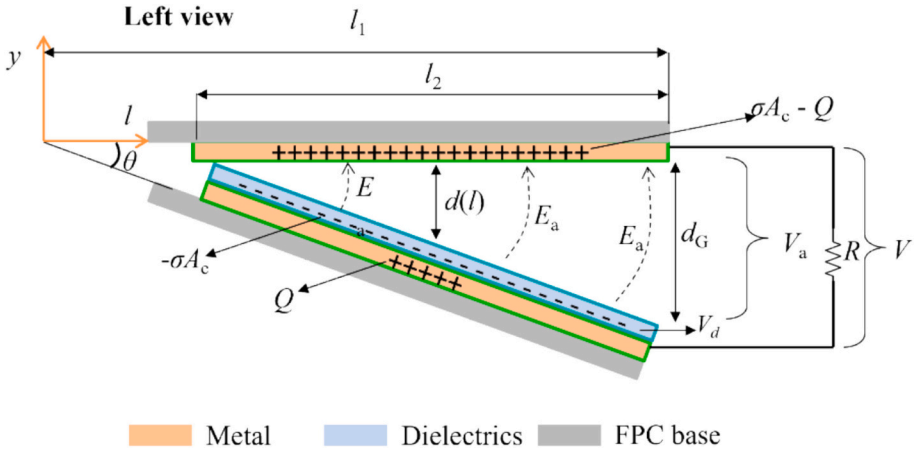

Fig. 2. Illustration of OTEH's electrical model.

$$A_c = \frac{Ll_2}{2} \tag{1}$$

where L is the base length of the isosceles triangle, and l_2 is its height. Because of the tribo-charges $-\sigma A_c$ on the FEP, the upper Cu layer acquires positive charges σA_c upon contact with the FEP layer. The air gap between the upper Cu layer and the FEP layer causes the lower Cu layer to acquire some of the positive charges, inducing a voltage potential V_a in the air gap, expressed as

$$W_e = \int_{l_1-l_2}^{l_1} \frac{\varepsilon_0 E_a^2}{2} w(l) dl \tag{2}$$

where W_e is the electrical energy in the air gap, l_1 is the distance from the origin to the vertex of the isosceles triangle, l_2 is the shortest distance from the base to the vertex, ε_0 is the permittivity of free space, and E_a is the electric field between the FEP and upper Cu layer. The term $w(l)$, representing the distance between the legs of the isosceles triangle parallel to its base depending on l, accounts for nonuniform side-to-side distances. Applying the equipotential assumption and triangle proportionality theorem, the electrical energy in the air gap is

$$W_e = \int_{l_1-l_2}^{l_1} \frac{L\varepsilon_0 V_a^2}{2l\theta(t)} \left(1 - \frac{l}{l_1}\right) dl = \frac{L\varepsilon_0 V_a^2}{2\theta(t)} \left[ln\left(\frac{l_1}{l_1 - l_2}\right) - \frac{l_2}{l_1}\right] \tag{3}$$

where $\theta(t)$ is the time-dependent separation angle between the two contact surfaces. Since the FEP and the upper Cu surfaces can be considered as two oppositely charged capacitor plates' surfaces [15], the electrical energy in the air gap can also be expressed as

$$W_e = \frac{CV_a^2}{2} \tag{4}$$

where C is the capacitance in the air gap derived as

$$C = \frac{\sigma A_c - Q(t)}{V_a} \tag{5}$$

Combining eqs. (3)–(5) results in an expression for V_a, which is

$$V_a = \frac{\theta(t)(\sigma A_c - Q(t))}{L\varepsilon_0 \left[ln\left(\frac{l_1}{l_1-l_2}\right) - \frac{l_2}{l_1}\right]} \approx \frac{d_G(t)(\sigma A_c - Q(t))}{l_1 L\varepsilon_0 \left[ln\left(\frac{l_1}{l_1-l_2}\right) - \frac{l_2}{l_1}\right]} \tag{6}$$

where $d_G(t)$ is the separation distance between the apices of the isosceles triangular contact surfaces. The small-angle assumption is used here. The FEP layer's negative surface charges and the positive surface charges on the lower Cu layer create a potential inside the FEP film. According to Gauss's Law, the potential inside the FEP dielectric is

$$V_d = -\frac{Q(t)h}{A_c\varepsilon_0\varepsilon_r} \tag{7}$$

where ε_r is the relative permittivity and h is the FEP layer thickness. Since the charges transfer across the resistor R, the voltage across is

$$V = R\frac{dQ(t)}{dt} \tag{8}$$

Kirchhoff's voltage law then relates eqs. (6)–(8) as

$$R\frac{dQ(t)}{dt} = \frac{\alpha d_G(t)(\sigma A_c - Q(t))}{Ll_1\varepsilon_0} - \frac{Q(t)h}{A_c\varepsilon_0\varepsilon_r} \tag{9}$$

where α is a geometric coefficient expressed as

$$\alpha = \left[ln\left(\frac{l_1}{l_1 - l_2}\right) - \frac{l_2}{l_1}\right]^{-1} \tag{10}$$

This results in the differential equation for the electrical model of a pair of isosceles triangular contact surfaces, referred to as a tribo-cell. For N tribo-cells in parallel on an OTEH, the total charge transferred through R is NQ. Therefore, the total voltage across R is

$$NR\frac{dQ(t)}{dt} = \frac{N\alpha d_G(t)(\sigma A_c - Q(t))}{Ll_1\varepsilon_0} - \frac{NQ(t)h}{A_c\varepsilon_0\varepsilon_r} \tag{11}$$

Eq. (11) is nonlinear, with $d_G(t)$ serving as the mechanical coupling term, depending on the contact-separation motion of the surfaces, which in turn depends on the OTEH's structural dynamics.

2.2. Mechanical model

As previously mentioned, $d_G(t)$ is the mechanical coupling term in the electrical model. Thus, a mechanical model describing the OTEH's dynamics under vertical vibration is necessary to simulate $d_G(t)$. Given the axial elasticity of the OTEH, its complex origami structure can be simplified into a spring-mass-damper system. The mechanical model, exemplified by the bellow-origami structure used by Chung et al. [34] is illustrated in Fig. 3. Here, the upper and lower triangular surfaces are fixed horizontally by rigid top and bottom substrates, respectively, with a mass block M attached to the top substrate. The separation distance between the apices of the triangular surfaces in a tribo-cell is $d_G(t)$, except for the top and bottom tribo-cells, where the distance is $\frac{d_G(t)}{2}$ due to the fixed horizontal orientation of the substrates. The differential equation for the top and bottom tribo-cells is

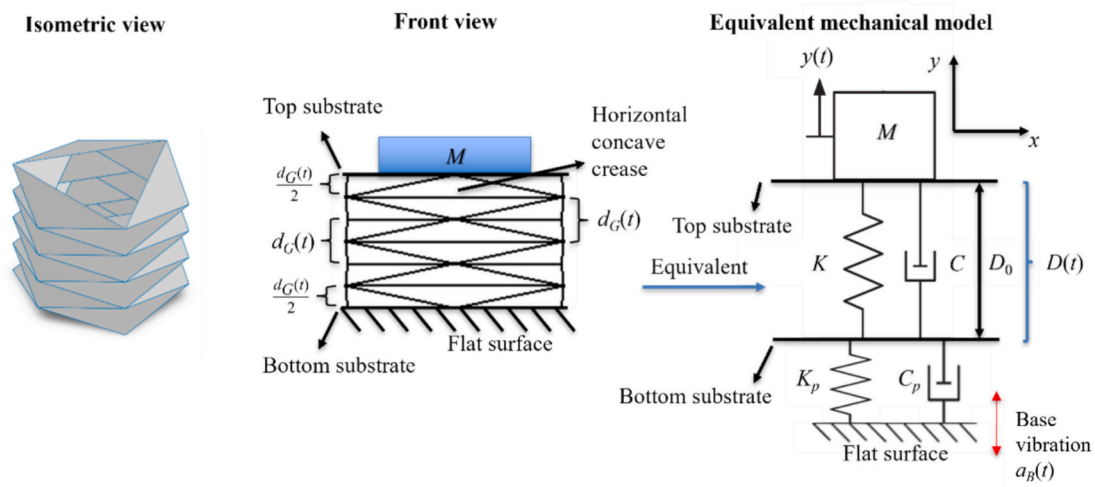

Fig. 3. Illustration of BOTEH's mechanical model.

$$R\frac{dQ_2(t)}{dt}=\frac{\alpha d_G(t)(\sigma A_c-Q_2(t))}{2Ll_1\varepsilon_0}-\frac{Q_2(t)h}{A_c\varepsilon_0\varepsilon_r} \tag{12}$$

In Fig. 3, the mechanical model simplifies the OTEH into a mass block M supported by a spring with stiffness K and a damper with a damping coefficient C. At equilibrium, the mass block's center is defined as the y-axis origin, with its vertical displacement denoted by $y(t)$. When subjected to vertical base vibration, the mass block's displacement can exceed D_0, the equilibrium distance between the bottom and top substrates, causing impact with the bottom substrate and subsequent rebound. An appropriate method is required to model this impact.

Although the bottom substrate of the OTEH is fixed on a flat surface in reality, it is modeled as a massless platform supported by a pseudo-spring with stiffness $K_p \gg K$ and a pseudo-damper with coefficient C_p. Since the bottom substrates and the flat surface are rigid, $K_p \gg K$ implies that the impact between the mass block and the bottom substrate is nearly rigid rather than elastic. This instantaneous sticking motion between the mass block and the substrate results in immediate rebounding due to elastic collision. The dynamics of the mass block under excitation acceleration $a_B(t)$ are described by the piecewise linear differential equation

$$M\ddot{y}(t)+C\dot{y}(t)+Ky(t)=\begin{cases}-Ma_B(t)\text{when } y(t)\geq -D_0\\ -Ma_B(t)-C_p\dot{y}(t)-K_py(t)\text{when } y(t)<-D_0\end{cases} \tag{13}$$

Since this equation describes the mass block's displacement $y(t)$ rather than the separation distance $d_G(t)$ of a tribo-cell, the relationship between $y(t)$ and $d_G(t)$ must be determined to solve the electrical model. The time-dependent distance between the top and bottom substrates, $D(t)$, is related to $d_G(t)$ as

$$D(t)=3d_G(t) \tag{14}$$

For the BOTEH and similar OTEHs, the number of horizontal creases a relates $D(t)$ and $d_G(t)$ as

$$D(t)=\frac{a-1}{2}d_G(t) \tag{15}$$

Because

$$D(t)=D_0+y(t) \tag{16}$$

where

$$D_0=\frac{a-1}{2}d_0 \tag{17}$$

Here, d_0 is the initial separation distance of a tribo-cell in the equilibrium state. Combining eqs. (15)–(17) results in the tribo-cell's separation distance between the triangular surfaces' apices

$$d_G(t)=d_0+\frac{2}{a-1}y(t) \tag{18}$$

Once $y(t)$ is solved, $d_G(t)$ in eq. (18) can be substituted into the electrical model in eq. (9) or (12) to determine the voltage across R for a single tribo-cell in Fig. 2. Although an electrostatic force may be induced in the air gap due to V_a, its influence on the mass block's displacement is often negligible in TEHs, as suggested by Fu et al. [40]. Thus, the electrostatic force is omitted from the simulation for simplicity.

3. Structural design and fabrication procedures of BOTEH

To experimentally validate the proposed electromechanical model for elastic OTEHs, this study uses the bellow-origami structure depicted in Fig. 3, previously applied in the literature. This section details the structural design and fabrication procedures of the BOTEH. The foundation of the BOTEH is the bellow-origami (BO) structure, constructed from a flexible yet durable printed circuit board (FPC) made of polyimide with 2D-printed copper (Cu) electrodes. In this study, the FPC sheet's dimensions are $W = 257.2$ mm by $H = 203.2$ mm. The FPC is divided into n rows by n - 1 valley-fold lines (in blue) and m columns by $m-1$ reference lines (in black), as shown in Fig. 4 (a). For this study, $n = 8$ and $m = 3$. The mountain-fold lines (in red) are diagonals of the rectangles formed by reference lines and the two vertical edge lines. The length lines of these rectangles span one column and are formed by valley lines and the two horizontal edge lines. After folding the valley and mountain lines, the sheet's vertical side edges are curled inward, as indicated by the arrows in Fig. 4 (a), until the edges meet and are taped together to form a cylinder.

Due to the pre-folded valley and mountain lines, creases form on the cylinder's surface, with mountain lines creating convex creases and valley lines forming concave creases. The BO structure's folding process and resulting top view are shown in Fig. 4 (b). The structure is naturally elastic and returns to equilibrium when released from a vertically stretched or compressed state, as illustrated in Fig. 4 (c). The cross-section, shown in Fig. 4 (c), is hexagonal but can vary by adjusting the number of columns, m. For instance, the cross-section becomes square when $m = 2$ and octagonal when $m = 4$.

Typically, a TEH contains a voltage generation unit (VGU) consisting of a tribo-pair with opposite charge affinities [15]. These materials acquire opposite charges through the triboelectric effect, and when bonded to metal electrodes connected to a resistor, electrostatic induction causes charge transfer between the electrodes upon separation. This

cyclic contact and separation induce an alternating current (AC) voltage. Therefore, material selection is crucial for fabricating the VGU. In this study, Cu and FEP polymer were chosen as the tribo-pair, with Cu serving as both the positive-charge-affined material and the electrode, while FEP, as the negative-charge-affined material, requires an additional bonded electrode.

The BOTEH's tribo-pair configuration is shown in Fig. 5 (a). The 2 *m*-th rows are covered with exposed Cu layers (ECuLs) interconnected by a narrow Cu strip on the left, while the (2 *m*–1)-th rows are covered with FEP layers over Cu layers interconnected by a narrow Cu strip on the right. The ECuLs are separate from the FEP-covered Cu layers (FCuLs), but the FCuLs can be connected to the ECuLs through external conducting wires to a resistor, *R*. This configuration is implemented on the FPC sheet, which is 2D-printed with Cu layers, as shown in Fig. 5 (b). Small dashed cuts are made along the mountain and valley-fold lines before adding the FEP layer to facilitate folding. Following the steps in Fig. 4 (a), the BOTEH prototype was obtained, as shown in Fig. 6.

In the BOTEH prototype, six triangular FR-4 plates are bonded to the top, overlapping the six triangular sections in Fig. 4 (b), forming a top substrate as depicted in Fig. 3. The same triangular plates are applied to the bottom to form the bottom substrate. The bottom substrate secures the BOTEH onto a seismic shaker's flat surface platform, while the top substrate holds a mass block *M* with a central hole. A guiding rod, with a diameter matching the central hole (3 mm), runs through the hole and is

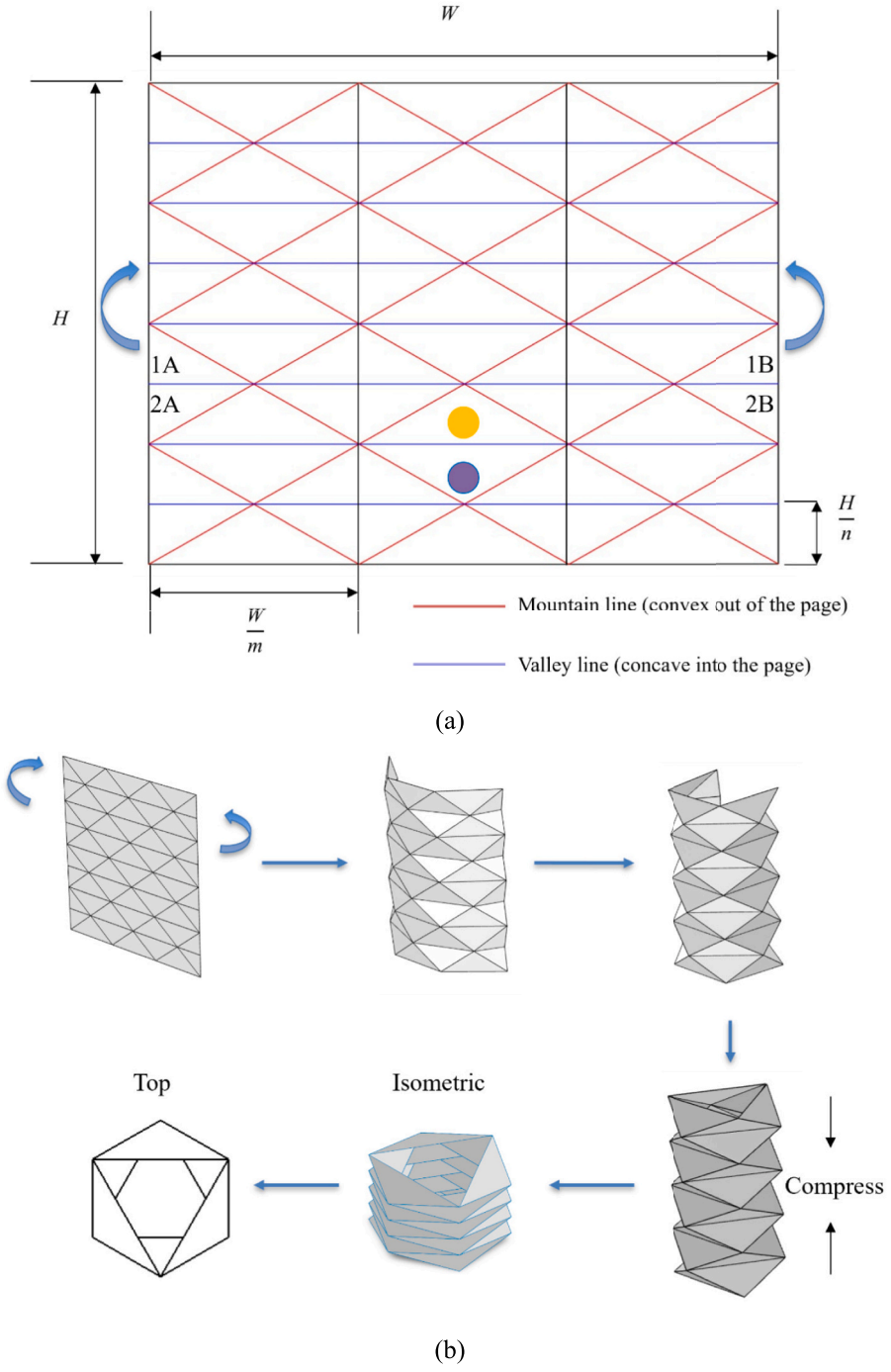

Fig. 4. (a) Folding line scheme of BO structure, (b) isometric view of BO structure's folding procedures and its top view, and (c) stretched, compressed, and equilibrium states of BO structure.

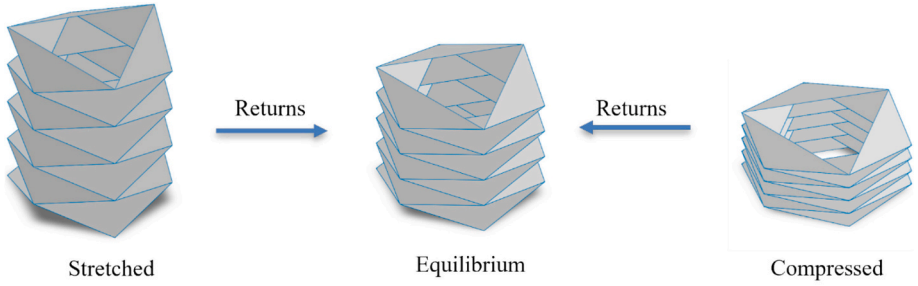

(c)

Fig. 4. (*continued*).

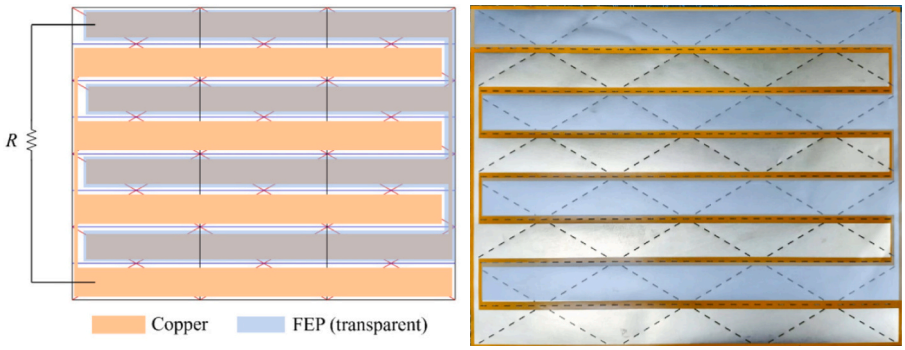

(a) (b)

Fig. 5. (a) Tribo-pair's schematic configuration, (b) actual FPC sheet with 2D-printed Cu electrodes, a tailored sticky FEP film, and dashed cuts that facilitate folding operations.

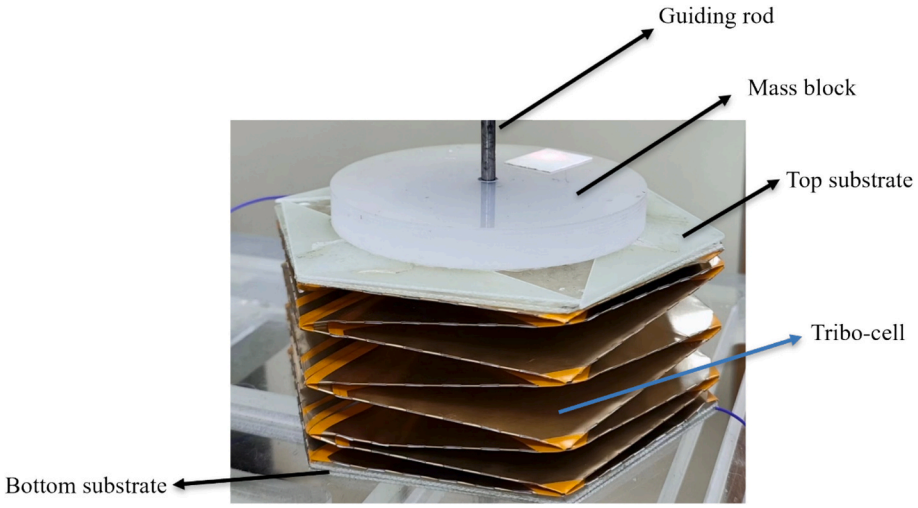

Fig. 6. BOTEH prototype with top and bottom substrates, a mass block with a central hole on the top substrate, and a guiding rod through mass block's central hole.

fixed vertically on the flat surface. When subjected to vertical forcing vibration from the seismic shaker, the BOTEH vibrates vertically without bending due to the guiding rod.

In the BOTEH prototype shown in Fig. 6, any pair of opposing isosceles triangular surfaces with overlapping bases is defined as a tribo-cell, as depicted in Fig. 1 (a), marked by the blue arrow. For example, on the unfolded sheet in Fig. 4 (a), the isosceles triangles marked by the blue and orange dots form such a tribo-cell. Additionally, any pair of right triangles sharing the same perpendiculars on the extreme left forms a tribo-cell with the corresponding pair of right triangles on the same rows on the extreme right. For example, the four right triangles marked 1 A, 1B, 2 A, and 2B in Fig. 4 (a). Triangles 1 A and 1B form an isosceles triangle similar to the one marked with the orange dot, while triangles 2 A and 2B form a triangle similar to the one marked with the blue dot once the sides of the sheet are curled inward and joined. The configuration in Fig. 5 indicates that each tribo-cell has one isosceles triangular surface covered by the ECuL and another by the FCuL. Additionally, since all ECuLs are interconnected but separate from the FCuLs, which are also interconnected, this configuration ensures that all tribo-cells are connected in parallel.

Table 1
Values of constants in the electrical model.

Parameters	Values
Number of rows on unfolded FPC sheet, n	8
Number of columns on unfolded FPC sheet, m	3
Length of unfolded FPC sheet, W (mm)	257.2
Width of unfolded FPC sheet, H (mm)	203.2
Area of triangular contact surfaces, A_c (mm^2)	1088.7
Thickness of FEP layer, h (mm)	0.003
Permittivity of free space, ε_0 (F/m)	$8.85418782 \times 10^{-12}$
Relative permittivity of FEP, ε_r	1.9
Geometric coefficient, α	0.0112

To simulate the BOTEH's response, the electromechanical model's governing equations must incorporate the bellow-origami structure's geometric coefficients. The base length of the triangular surfaces, L, in eq. (11) corresponds to the width of a column, $\frac{W}{m}$, in Fig. 4 (a) while the height of the triangular surfaces, l_1, corresponds to the width of a row, $\frac{H}{n}$. The electrical model's governing eq. (11) can then be modified as

$$NR\frac{dQ(t)}{dt} = \frac{mnN\alpha d_G(t)(\sigma A_c - Q(t))}{WH\varepsilon_0} - \frac{NQ(t)h}{A_c\varepsilon_0\varepsilon_r} \tag{19}$$

where

$$\alpha = \left[ln\left(\frac{nH}{nH - n^2 l_2}\right) - \frac{nl_2}{H}\right]^{-1} \tag{20}$$

With the configuration of the BOTEH used in this study, $m = 3$ and $n = 8$. The number of columns, m, can be adjusted so that eq. (19) fits BOTEHs with different cross-sections. Additionally, the configuration in Fig. 4 (a) results in $m(n-1)$ tribo-cells, 2 m of which are the top and bottom tribo-cells. In this study, there are 6 top-and-bottom tribo-cells and 15 tribo-cells in between. Therefore, as long as $n \geq 3$, combining eqs. (12) and (19) gives the total voltage across R as

$$2mR\frac{dQ_2(t)}{dt} + m(n-3)\frac{dQ(t)}{dt} \tag{21}$$

Table 1 summarizes the constant values used in this study's electrical model in eqs. (19) and (20).

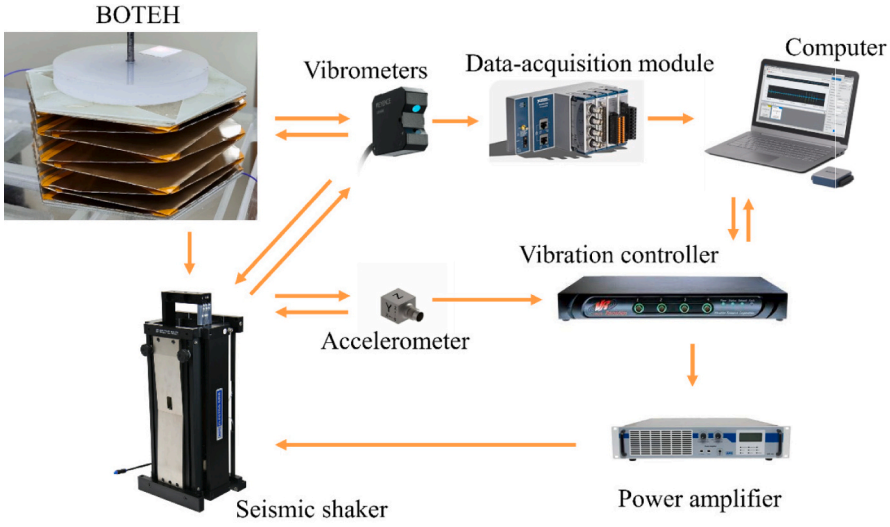

(a)

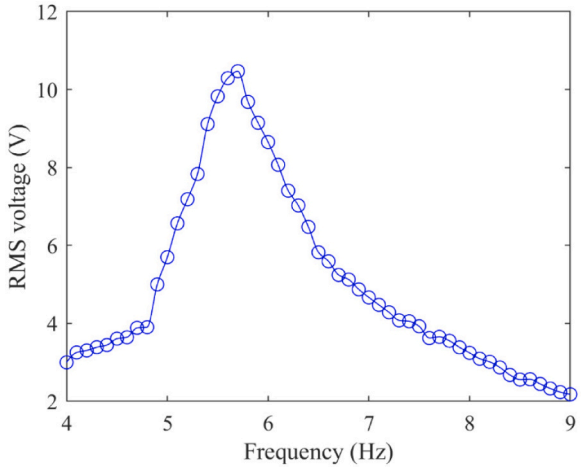

(b)

Fig. 7. (a) Preliminary experimental setup for determining the BOTEH's natural frequency and (b) RMS displacement response of mass block in the frequency domain when excitation acceleration was fixed at 0.4 g.

4. Validation of proposed model

4.1. Experimentally determined electromechanical parameters

Before the experimental validation of the proposed electromechanical model can be conducted, a few undetermined parameters in the governing equations must be obtained from preliminary experiments. The first parameter to be determined is the damped natural frequency f_d of the BOTEH under the mass load M. Due to the complexity of the BO structure, an analytical calculation of the damped natural frequency is hardly feasible. However, it is straightforward to determine it experimentally. The setup for determining f_d is shown in Fig. 7 (a). First, the BOTEH is placed on a seismic shaker's platform. The seismic shaker provides the BOTEH with vertical base vibration controlled by a vibration controller, whose control signals are sent to the shaker after being amplified by a power amplifier. An accelerometer is placed on the shaker's platform to measure the platform's real-time vertical acceleration and send the output signals to the vibration controller, which then controls the shaker's acceleration so it operates at the user's preset vibration acceleration. The vibration controller is connected to a computer's control software, with which the user can adjust different vibratory parameters such as frequency and excitation acceleration. A pair of laser vibrometers is used to measure the vertical displacement of the BOTEH's mass block under vibration. The vibrometers' output signals are collected by a data-acquisition module (DAQ). The DAQ is connected to the computer's signal-viewing software and displays the measured displacement waveform.

Through the vibration controller, a frequency sweep from 4 Hz to 9 Hz at a 0.4 g excitation acceleration was applied to the shaker. The acceleration was chosen at 0.4 g to ensure no impact event was involved when determining the BO structure's damped natural frequency, and the mass block would not impact the bottom substrate during the sweep. The root-mean-squared (RMS) displacement response of the mass block was recorded and is shown in Fig. 7 (b). The maximum RMS displacement occurs at $f_d = 5.6$ Hz, corresponding to the mass $M = 42.5$ g. The damped natural frequency f_d can be tuned by changing the mass M because of the relationship $2\pi f_n = \sqrt{\frac{K}{M}}$. The particular $M = 42.5$ g was chosen for demonstration purposes. Additionally, with $M = 42.5$ g, the mass block will impact the bottom substrate at higher excitations, facilitating subsequent experimental validations.

To determine the stiffness K of the structure, one must determine the undamped natural frequency f_n at 0.4 g excitation, which requires the knowledge of the damping ratio ζ. The next parameter to be determined is ζ at 0.4 g excitation, which involves the logarithmic decrement method that requires data on the displacement decay response of the mass block under a certain excitation after the forcing vibration stops. The decay response of the mass block's displacement under 5.6 Hz forcing frequency and 0.4 g excitation is shown in Fig. 8 (a) below. At around 1.5 s, the vibration from the shaker was halted, and the magnitude of the mass block's displacement started decaying. The peak displacement values used in the calculation are marked by the red circles in Fig. 8 (a), resulting in the damping ratio ζ being 0.0619. Because of the relationship $f_n = \frac{f_d}{\sqrt{1-\zeta^2}}$, the undamped natural frequency f_n is roughly 5.61 Hz. The stiffness K is thus 52.7785 N/m. The relationship between the damping coefficient and the damping ratio $C = 2\zeta\sqrt{KM}$ results in C being 0.1852 Ns/m at 5.6 Hz forcing frequency and 0.4 g excitation. The values of C at different forcing frequencies and excitations are calculated for subsequent model simulation and validation using the same method because later experimental validations will be conducted from 0.5 g excitation to 0.8 g excitation with a frequency sweep range from 4 Hz to 9 Hz. These selected vibration conditions (4 Hz–9 Hz, 0.4 g–0.8 g) were chosen to align with typical low-frequency ambient vibrations found in real-world applications, such as structural vibrations in buildings, bridges, and machinery [41]. These frequencies, usually below 50 Hz, and acceleration ranges, often less than 1 g, are commonly observed in practical energy harvesting scenarios, particularly for powering low-power IoT devices [41,42]. Therefore, the BOTEH prototype used for the experimental validation of the electromechanical model is tuned to operate within these specified vibration conditions. The results of the experimentally determined C at different excitations and forcing frequencies are shown in Fig. 8 (b). The damping coefficient varies irregularly with frequency at each excitation, which is the result of unpredictable friction between the guiding rod and the mass block. However, a trend can be observed that C decreases after about 5.5 Hz, which could be due to the effect of friction between the mass block and the guiding rod diminishing as the forcing frequency increases.

In addition to the mechanical parameters determined above, the areal electric charge density σ in eq. (12) must also be quantified through experiments as it depends on the ambient environment conditions such as humidity and temperature. Since vibratory conditions can affect the completeness of contact between the tribo-pair and how much the pair separates, influencing the amount of maximum transferred charge that might not equal σA_c as shown in Fig. 2, accurately determining the amount of accumulated charge on the dielectric FEP layer is challenging and demands extremely precise equipment. Instead, the maximum transferred charge Q_{max} at each excitation was measured and assumed to be approximately equal to σA_c. The areal charge density σ was then determined by $Q_{max} \approx \sigma A_c$. To experimentally measure Q_{max}, the output electrodes of the BOTEH were connected to an electrometer capable of measuring transferred charge. The BOTEH was given vibration excitations from 0.5 g to 0.8 g at 0.1 g increments. The forcing

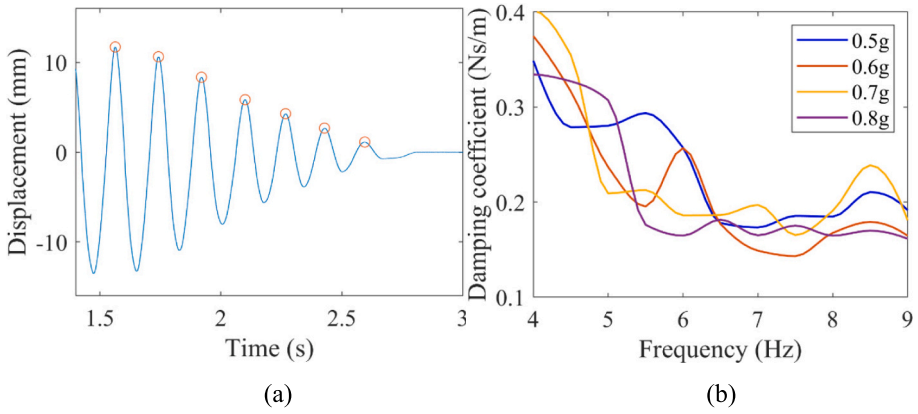

Fig. 8. (a) Decay of mass block's displacement at 5.6 Hz and 0.4 g, and (b) experimentally determined damping coefficients at different forcing frequencies and excitations.

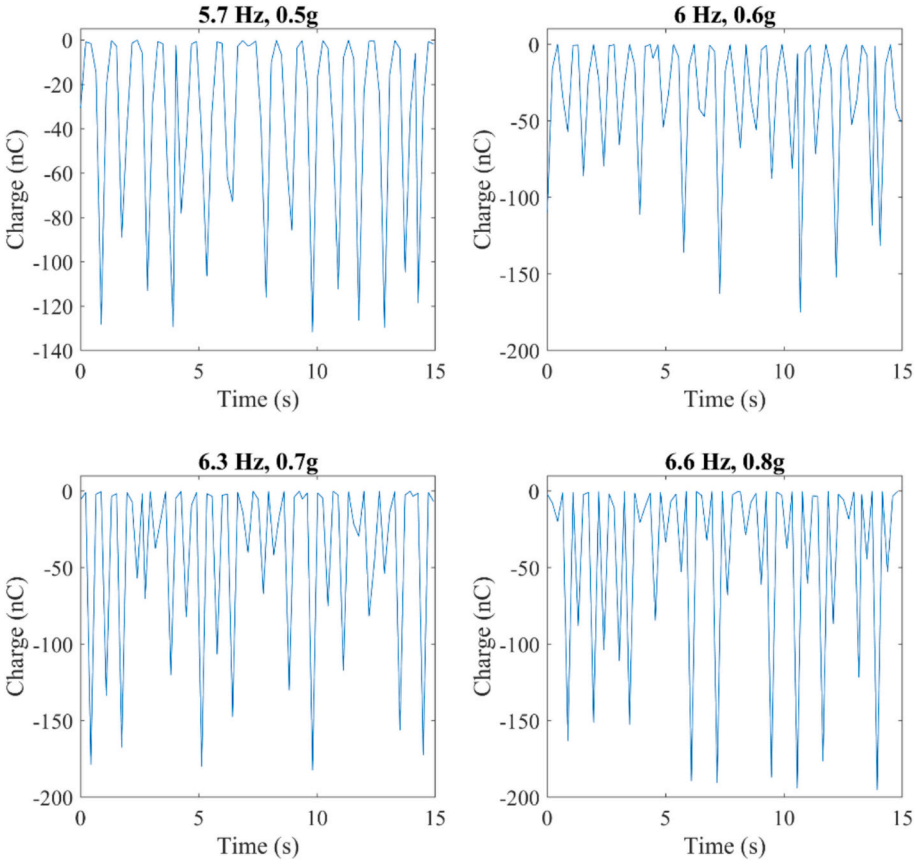

Fig. 9. Maximum transferred charge at different excitation levels.

Table 2
Values of experimentally determined electromechanical parameters used in the model.

Parameters	Values
Damped natural frequency of BOTEH, f_d (Hz)	5.60
Undamped natural frequency of BOTEH, f_n (Hz)	5.61
Areal surface charge density, σ, at 0.5 g (nC/mm^2)	5.15
Areal surface charge density, σ, at 0.6 g (nC/mm^2)	6.84
Areal surface charge density, σ, at 0.7 g (nC/mm^2)	7.13
Areal surface charge density, σ, at 0.8 g (nC/mm^2)	7.63

frequency was varied at each excitation to find the frequency at which the maximum transferred charge occurred. The charge transfer plots at each excitation under the forcing frequency at which Q_{max} occurs are shown in Fig. 9. The maximum peak value corresponds to Q_{max}. Because the maximum sampling rate of the electrometer is low, it is necessary to let the shaker operate for about 15 s to ensure the maximum charge value is recorded. The maximum transferred charge Q_{max} values are 131.7 nC, 175.0 nC, 182.4 nC, and 195.3 nC at 5.7 Hz – 0.5 g, 6 Hz – 0.6 g, 6.3 Hz – 0.7 g, and 6.6 Hz – 0.8 g, respectively. The areal surface charge densities at each excitation can then be determined from $Q_{max} \approx \sigma A_c$. Table 2 summarizes the experimentally determined electromechanical parameters in this subsection, except for the damping coefficients under different vibratory conditions shown in Fig. 8 (b).

4.2. Experimental validation of electromechanical model

Once the necessary electromechanical parameters have been determined, the output responses from the electromechanical model can be simulated. The simulation was conducted in MATLAB's programming environment using the ODE23TB differential equation solver, which is well-suited for solving stiff differential equations.

Before performing experimental validation, the key parameter affecting the nonlinear impact dynamics, K_p, must first be determined. From the analysis of the BOTEH's mechanical model in Section 2.2, it is evident that the nonlinear impact dynamics arise from the interaction between the proof mass block M, bonded to the top substrate, and the bottom substrate, which is attached to the rigid flat surface of the seismic shaker platform. In reality, the bottom substrate behaves as a rigid surface, preventing mid-impact sticking motion between the mass block and the bottom substrate. As a result, the mass block immediately rebounds upward after impact. To accurately model this behavior, K_p is assumed to be very stiff and near-rigid, ensuring that any mid-impact sticking motion between the mass block and the bottom substrate is instantaneous. Consequently, $K_p \gg K$.

To satisfy this condition, reasonable values of K_p should exceed 500 N/m—approximately ten times the value of K. To determine an appropriate K_p, we first set the model parameters based on the experimentally determined electromechanical properties to maximize charge transfer, which occurs at an excitation acceleration of 0.8 g and a frequency of 6.6 Hz. These vibration parameters were chosen to ensure that the selected K_p is sufficiently large to prevent mid-impact sticking motion for excitation accelerations up to 0.8 g.

A phase diagram depicting one period of steady-state vibration at different values of K_p (with C_p fixed at an empirical value of 0.1 Ns/m) is shown in Fig. 10 (a). The results reveal an abrupt change in velocity when the displacement y approaches −21 mm, indicating the moment when the mass block impacts the bottom substrate and then rebounds. The influence of different K_p values on the impact dynamics is further detailed in Fig. 10 (b).

In Fig. 10 (b), impact occurs at $y = -D_0 = -21$ mm, with mid-impact sticking motion observed when $y < -21$ mm. For lower values of K_p (~500 N/m), significant sticking motion is evident, as indicated by y

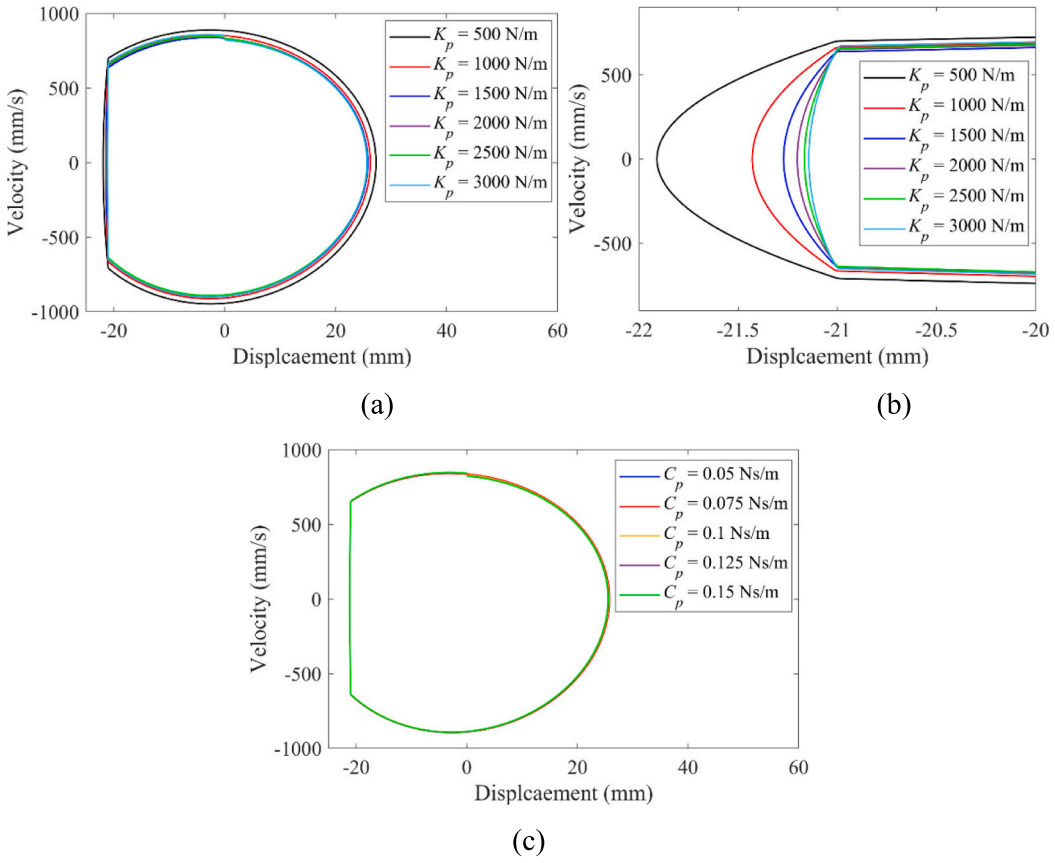

Fig. 10. (a) Simulated phase diagram of the BOTEH when under 0.8 g and 6.6 Hz of excitation with different values of K_p while C_p is fixed at 0.1 Ns/m. (b) Phase plot showing detailed impact dynamics when different K_p's are applied in model simulation. (c) Phase diagram with different C_p's applied while K_p = 2500 N/m.

descending beyond −21 mm, exceeding the initial separation distance D_0. However, as K_p increases, mid-impact sticking motion becomes negligible. When K_p reaches 3000 N/m, the sticking motion is minimal, similar to the case when K_p = 2500 N/m. While 3000 N/m K_p would be an ideal choice, MATLAB's numerical solver encounters difficulties at this value, so we set K_p at 2500 N/m, a value significantly larger than the experimentally determined axial stiffness of the BOTEH, K = 52.7785 N/m.

A similar investigation was conducted to determine an appropriate damping coefficient C_p. A phase plot depicting one period of steady-state vibration under 0.8 g and 6.6 Hz forcing vibration with K_p fixed at 2500 N/m is shown in Fig. 10 (c). The results indicate that varying C_p has negligible effects on the impact dynamics of the BOTEH. Therefore, we retained the empirical value of C_p = 0.1 Ns/m in the model.

With the correct parameter input, the first response simulated is the time-domain voltage-displacement output across the external resistor R. The experimental time-domain voltage response was recorded using an oscilloscope connected to the BOTEH's output electrodes. Because the oscilloscope's input channel has a built-in impedance of 100 MΩ, the value of R was set to 100 MΩ in the simulation program. The time-domain displacement response of the mass block M was collected using vibrometers. To validate the model's ability to correctly predict the time-domain responses under different vibratory conditions, response data were collected when the BOTEH was given a range of excitations from 0.5 g to 0.8 g in 0.1 g increments. Additionally, at each excitation, the forcing frequency was set to be the frequency at which the maximum charge transfer occurred, as shown in Fig. 9. The results of the simulated and experimental time-domain voltage and displacement responses are shown in Fig. 11. It can be seen that the experimental results converge well with the simulated results. The model captures the correct magnitudes of the output voltage and the mass block's displacement in the time domain under different excitations. It is worth noting that the experimental voltage responses are slightly noisy and contain minor secondary peaks. This is due to the fact that, when the BOTEH is in operation, not every pair of triangular contact surfaces can contact and separate simultaneously in a perfectly synchronized manner because of fabrication imperfections.

Since the forcing frequency at each excitation level in Fig. 11 is chosen to maximize charge transfer, as indicated in Fig. 9 the peak voltage $V(t)$ and displacement $y(t)$ in Fig. 11 reach their highest magnitudes for each respective excitation level. This behavior can be deduced from Eq. (19), where the output voltage on the left-hand side is approximately proportional to the separation distance minus the product of the separation distance and transferred charge ($V(t) \propto d_G(t)$ - $d_G(t)$ $Q(t)$). As excitation increases, $d_G(t)$ grows due to greater input kinetic energy, while $Q(t)$ also increases due to a larger effective triboelectric surface charge density resulting from more complete contact. Given that $Q(t) \leq 0$ (as shown in Fig. 9) and $d_G(t) \geq 0$, their combined effect produces the largest output voltage at each excitation level.

A comparison of the maximum and minimum peak values of $V(t)$ and $y(t)$ across different excitation levels—both experimental and simulated—is shown in Fig. 12. The results confirm that $d_G(t)$ increases with excitation, as indicated by the increasing positive peak values of $y(t)$. The negative peaks of $y(t)$ (y_{min}) occur when the mass M impacts the bottom substrate (Fig. 3), meaning their magnitudes should consistently equal D_0 = 21 mm, the initial separation distance between M and the bottom substrate. However, the experimental y_{min} values are generally larger than the simulated ones. This discrepancy arises because, during vibration, the BOTEH prototype does not ensure the perfect and simultaneous contact and separation of all tribo-cells due to fabrication tolerances. As a result, the BOTEH could not fully compress in the experiment, preventing M from reaching $y(t) = -D_0$.

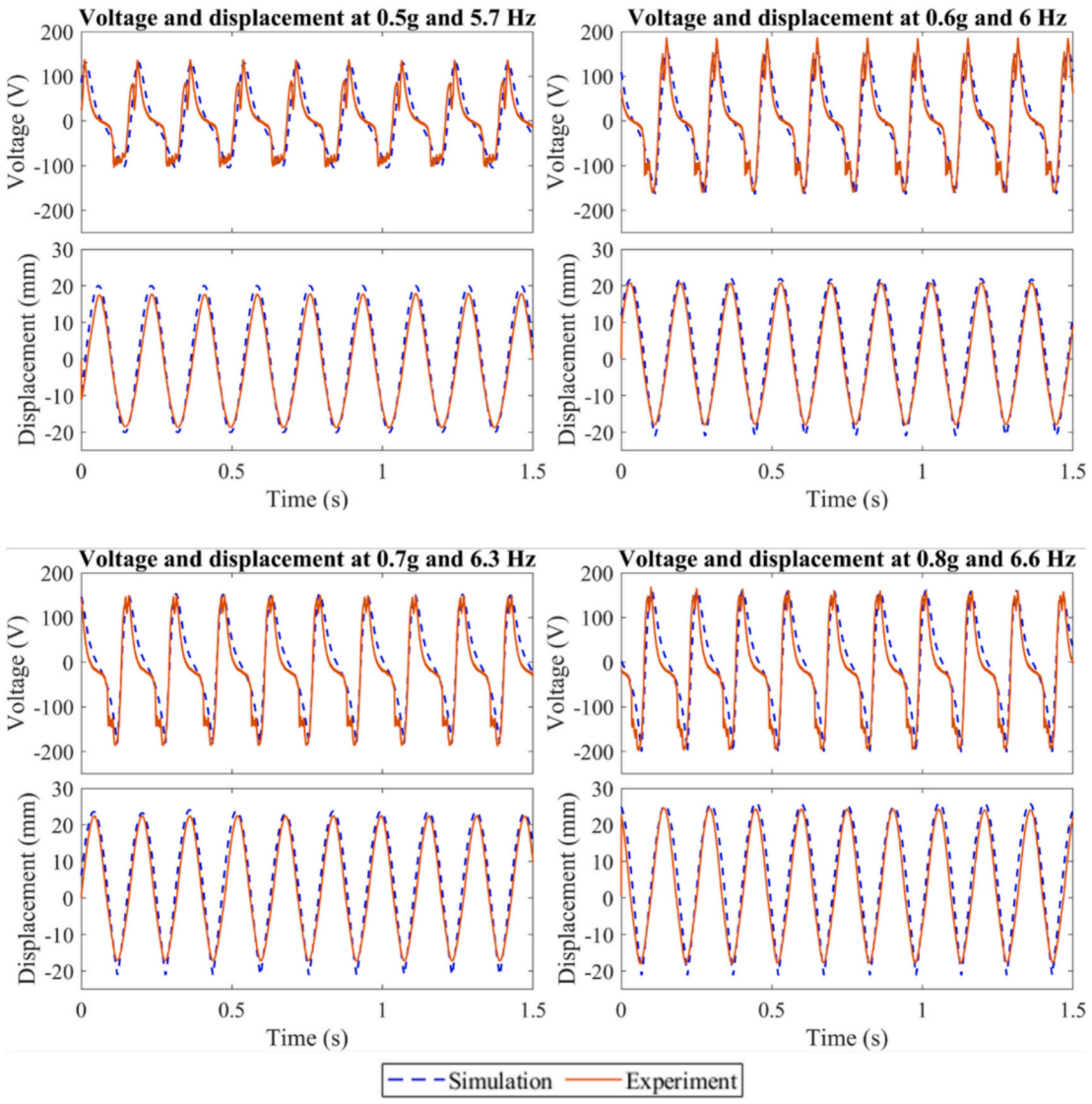

Fig. 11. Simulated and experimental time-domain voltage and displacement responses of BOTEH.

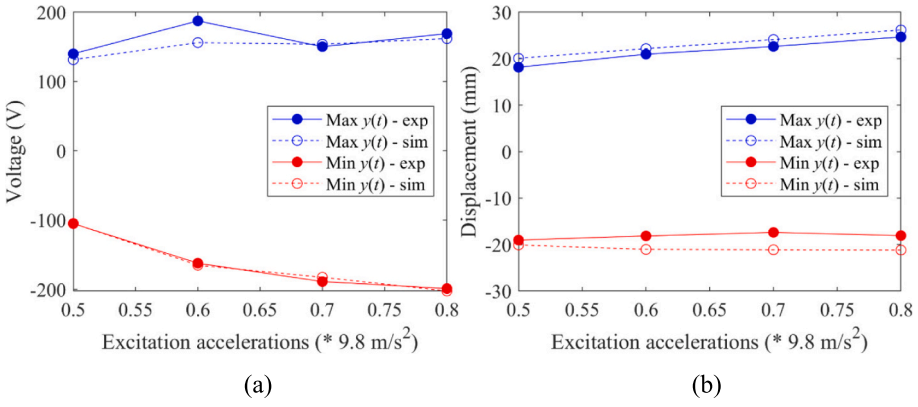

Fig. 12. Experimental and simulated maximum and minimum peak voltage and displacement of BOTEH in time domain given different excitation levels.

Fig. 12 also confirms that $|V(t)|$ generally increases with excitation. However, the positive peak $V(t)$ at 0.6 g deviates significantly from the simulated result due to an abnormal double positive peak in a single period of the voltage plot at 0.6 g in Fig. 11. These secondary peaks are not limited to extrema—they also appear slightly to the left of the negative peaks. This irregularity is again attributed to the unsynchronized contact and separation of certain tribo-cells during the experiment. For instance, while most tribo-cells remain open, one or two might

close earlier than the others, leading to these abnormal secondary peaks.

Additionally, the model can be used to interpret the nonlinear electromechanical dynamics of the BOTEH. It can be seen from Fig. 11 that, at the negative peak in the displacement response, the voltage reaches the minimum first and then quickly rises to the maximum before the displacement reaches the maximum, as illustrated more clearly in Fig. 13. Here, two periods of the simulated time-domain voltage and displacement responses when the BOTEH is under 0.6 g of excitation and 6 Hz of forcing frequency are shown. To interpret how the displacement of the mass block influences the voltage output, one period of the voltage-displacement response in Fig. 13 is divided into three stages. During stage 1, the BOTEH compresses from the stretched state to its fully compressed state, driving the separation distance between the tribo-pair from the maximum to zero. The negative charges transfer from the upper Cu electrode to the lower one depicted in Fig. 1 (b) during this stage, so the voltage, which is the rate of charge transfer, reaches the minimum. During stage 2, the BOTEH starts stretching out, leading to the separation between the tribo-pair. In this stage, positive charges transfer from the upper Cu electrode to the lower, resulting in the voltage quickly rising to the maximum. However, as the BOTEH keeps stretching, the positive charge transfer slows down until it stops in stage 3, resulting in the voltage dropping from the maximum to zero.

Besides the time-domain electromechanical response, the proposed

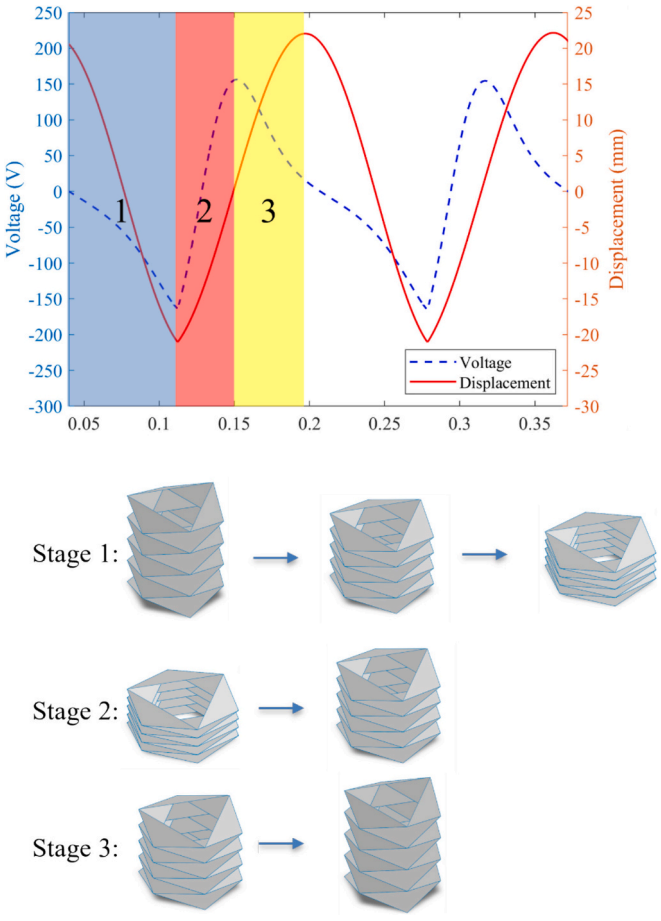

Fig. 13. Three stages in a period of BOTEH's time-domain simulated voltage-displacement response.

model's ability to predict the frequency-domain response was also validated. At each base excitation level from 0.5 g to 0.8 g in 0.1 g increments, a frequency sweep from 4 Hz to 9 Hz was applied to the BOTEH, and the RMS voltage (V_{rms}) from the BOTEH and the RMS displacement (y_{rms}) of the mass block were recorded both in the simulation and the experiment. In the experiment, the RMS values were obtained from the RMS computation algorithm built into the oscilloscope, while the simulated RMS values were computed with the built-in RMS computation function in MATLAB. The results are shown in Fig. 14. Notably, the frequencies at which the maximum RMS displacement and voltage occur at each excitation level correspond to the frequencies where the maximum charge transfer is observed, as shown in Fig. 9. These frequencies represent the shifted natural frequencies, which increase with higher excitation levels due to the nonlinear dynamics of the BOTEH. This shift occurs because greater excitation leads to stronger impacts on the mass block, effectively stiffening the overall structure under forced vibration and causing the natural frequency to shift to the right. Additionally, V_{rms} increases with increasing y_{rms}. This relationship can be explained by the fact that greater input kinetic energy results in larger displacement magnitudes, enabling more energy to be converted into electrical energy, which manifests as a higher voltage output.

Another key observation from Fig. 14 is the rate of increase of V_{rms} and y_{rms}. In general, these values initially rise at a high rate before the rate of increase abruptly drops at a certain frequency, f, until the forcing frequency surpasses the shifted natural frequency (f_s), after which both V_{rms} and y_{rms} begin to decrease sharply. For instance, at 0.8 g excitation, V_{rms} and y_{rms} increase rapidly starting from $f = 4$ but their growth rate suddenly declines around 4.7 Hz. Between $f = 4.7$ Hz and $f_s = 6.6$ Hz, the increase remains minimal. Once f surpasses $f_s = 6.6$ Hz, both V_{rms} and y_{rms} begin to drop abruptly. Similar trends are observed at other excitation levels, despite some noise and instability in the responses. The frequency range in which the rate of increase remains low corresponds to the contact interval (CI), during which the triboelectric surfaces of the BOTEH begin making contact. This CI is centered around the system's undamped natural frequency, f_n, because $|y(t)|$ is larger and ensures contact between the triboelectric surfaces when the system is closer to resonance. Furthermore, at higher excitation levels, $|y(t)|$ is also larger even when off-resonance, allowing contact between triboelectric surfaces across a broader frequency range. As a result, the CI widens at higher excitation levels.

The reason why the rate of increase of y_{rms} slows down within the CI, compared to the region before it, is that in this interval, the mass M starts making contact with the bottom substrate, causing $y(t)$ to reach its negative extremum. At higher f near the shifted natural frequency f_s, $y(t)$ does not go below $-D_0$, as shown in Fig. 12 (b). However, at slightly higher frequencies within the CI, the positive peaks of $y(t)$ can still increase slightly as the forcing frequency approaches f_s, which is also evidenced in Fig. 12 (b). Consequently, both y_{rms} and V_{rms} continue to rise, albeit at a reduced rate within the CI. However, once f surpasses f_s, y (t) decreases to the extent that the triboelectric surfaces can no longer make contact. This abrupt transition from a contact-separation state at resonance to a fully separated off-resonance state significantly reduces charge transfer, causing V_{rms} to drop suddenly as well.

In general, the simulated RMS responses in the frequency domain match considerably well with the experimental results. The experimental and simulated RMS displacement responses agree with each other particularly well, as evidenced by the fact that both the RMS displacement magnitude and the response frequency bandwidth are correctly predicted. Although the experimental RMS voltage response seems less aligned with the simulated result, which is mainly due to imperfect and non-ideal experimental conditions stemming from loose fabrication tolerances of the BOTEH, the disparity is still minor as it

mainly occurs at off-resonance frequencies. Because the magnitude and the operating bandwidth of the RMS voltage are still decently well-predicted, the model serves as an excellent tool for estimating the frequency-domain voltage response.

4.3. Equivalent circuit model validation of electromechanical model

The analytical solutions to the electrical governing equation in Eq. (9) contain several complex integrals, including nested integrals and integrals with nonlinear mechanical coupling terms, as shown by the expression for the transferred charge, $Q(t)$, below

$$Q(t) = \left[\int_0^t \frac{\sigma A_c \alpha d_G(t)}{RLl_1\varepsilon_0} e^{\int_0^\tau \frac{\alpha A_c \varepsilon_r d_G(t)+hLl_1}{RLl_1 A_c \varepsilon_0 \varepsilon_r} dz} d\tau \right] e^{-\int_0^t \frac{\alpha A_c \varepsilon_r d_G(t)+hLl_1}{RLl_1 A_c \varepsilon_0 \varepsilon_r}} \tag{22}$$

The expression for the voltage is then

$$V(t) = \frac{\sigma A_c \alpha d_G(t)}{Ll_1\varepsilon_0} - \frac{\alpha A_c \varepsilon_r d_G(z) + hLl_1}{Ll_1 A_c \varepsilon_0 \varepsilon_r} e^{-\int_0^t \frac{\alpha A_c \varepsilon_r d_G(\tau)+hLl_1}{RLl_1 A_c \varepsilon_0 \varepsilon_r}} \int_0^t \frac{\sigma A_c \alpha d_G(\tau)}{RLl_1\varepsilon_0} e^{\int_0^\tau \frac{\alpha A_c \varepsilon_r d_G(z)+hLl_1}{RLl_1 A_c \varepsilon_0 \varepsilon_r} dz} d\tau \tag{23}$$

As a result, deriving explicit analytical results is highly impractical. This is the reason why the theoretical governing equations are numerically solved using MATLAB in this study, which is a widely adopted approach for solving the governing equations of TEHs. The numerically solved theoretical predictions are then validated experimentally above to ensure the accuracy of the model. To further validate the proposed electromechanical model using the BOTEH as an example, an alternative simulation approach can be explored and compared with the current theoretical predictions. One promising option is the equivalent circuit model (ECM) of BOTEH's electromechanical system. An ECM represents a physical system using circuit components such as resistors, capacitors, inductors, and voltage sources, effectively capturing its key behaviors [43,44]. ECMs are widely used in piezoelectric energy harvesting, as they enable complex electromechanical systems like piezoelectric energy harvesters to be analyzed and simulated using circuit analysis techniques [45,46]. Given that the BOTEH is also a complex nonlinear electromechanical system, an ECM can be established and compared

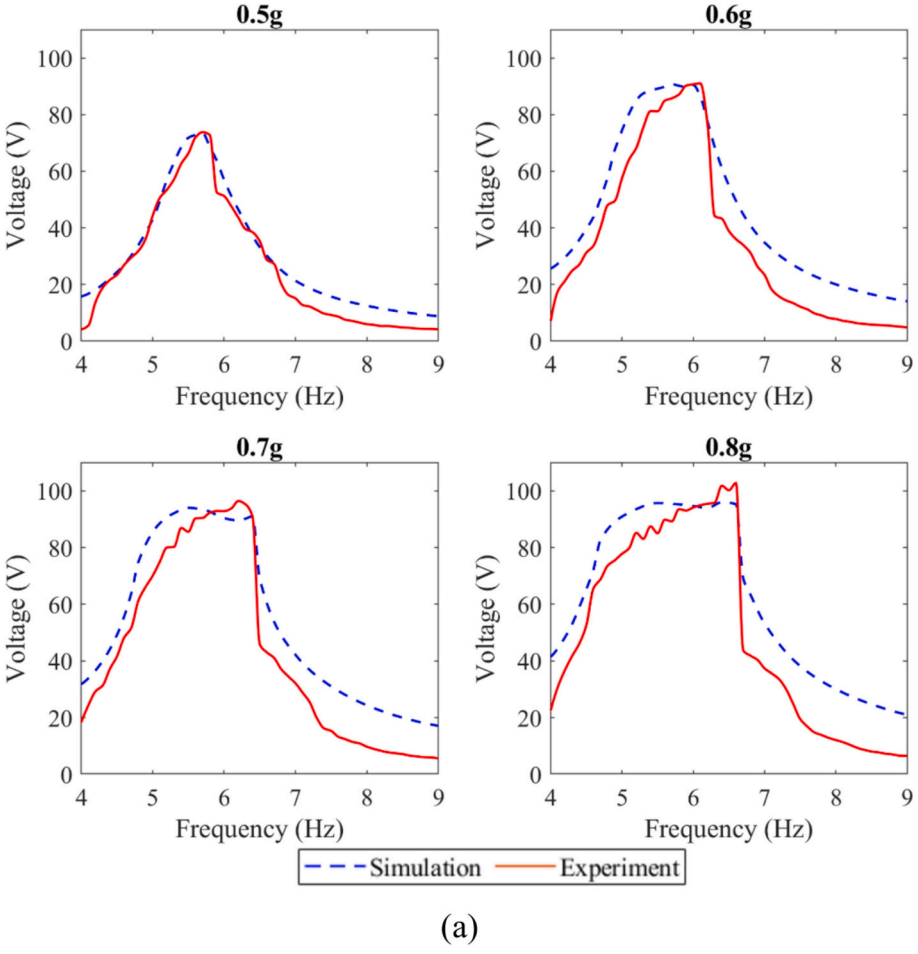

Fig. 14. (a) RMS voltage response and (b) RMS displacement response of BOTEH in the frequency domain.

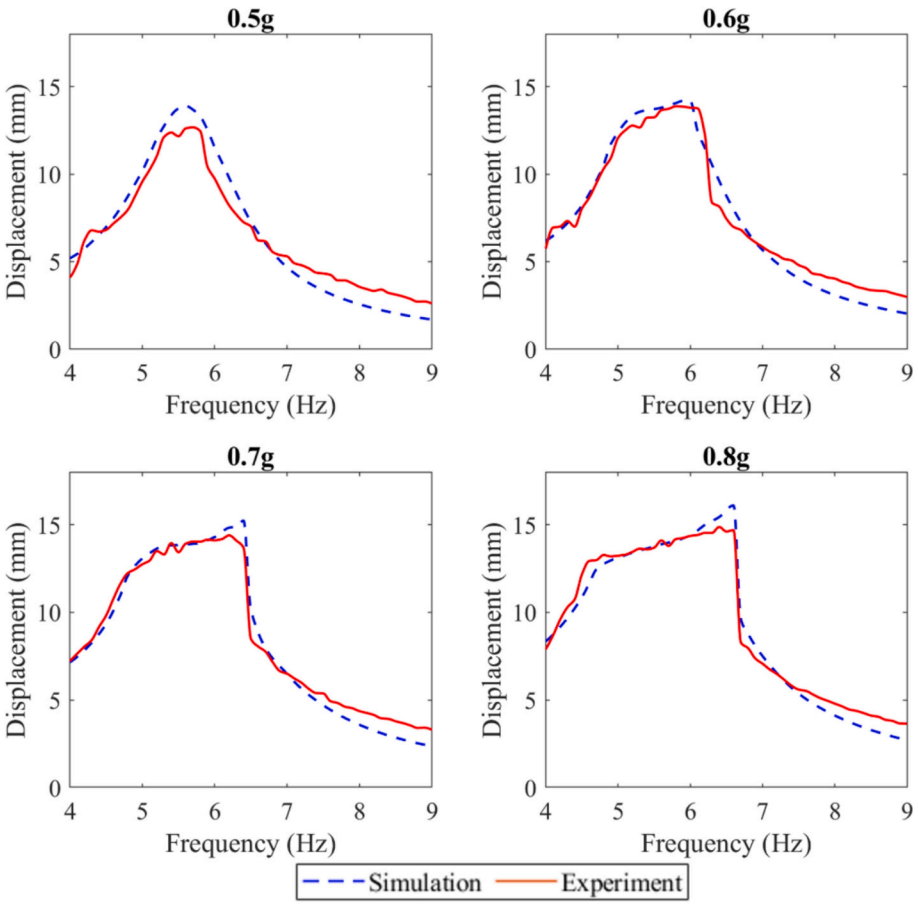

Fig. 14. (*continued*).

with the theoretical predictions.

The key to developing an ECM for the BOTEH is identifying circuit components that correspond to its mechanical and electrical parameters. The mechanical governing equation in Eq. (13) can be interpreted as a forced resistor-inductor-capacitor (RLC) oscillator, expressed as

$$L_{eq}\frac{d^2}{dt^2}q(t)+R_{eq}\frac{d}{dt}q(t)+\frac{1}{C_{eq}}q(t)=V_N(t) \tag{24}$$

where $q(t)$ represents the pseudo-charge equivalent to the displacement $y(t)$, L_{eq} is the pseudo-inductor corresponding to the mass M, R_{eq} is the pseudo-resistor equivalent to the damping coefficient C, C_{eq} is the pseudo-capacitor corresponding to the inverse of BOTEH's stiffness K,

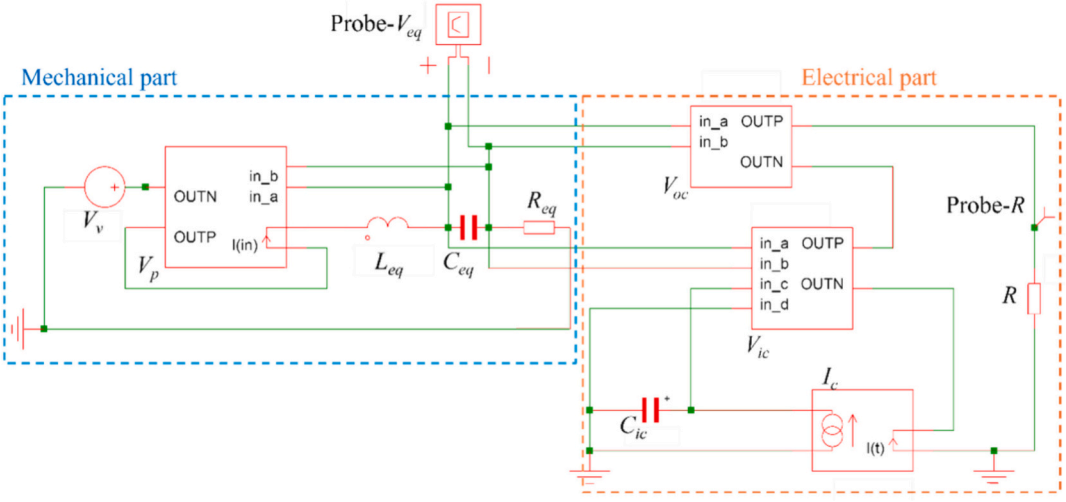

Fig. 15. ECM of one tribo-cell's electromechanical model for BOTEH.

and $V_N(t)$ is the pseudo-voltage source representing the external force on the right-hand side of Eq. (13). The pseudo-voltage source can be further expressed as

$$V_N(t) = V_v(t) + V_p(t) \tag{25}$$

where $V_v(t)$ corresponds to the base excitation displacement -$Ma_B(t)$, and $V_p(t)$ represents the nonlinear impact force $F_p(t)$, given by

$$F_p(t) = \begin{cases} 0 \text{when } y(t) \geq -D_0 \\ -C_p\dot{y}(t) - K_p y(t) \text{when } y(t) < -D_0 \end{cases} \tag{26}$$

Thus, $V_v(t)$ and $V_p(t)$ are respectively defined as

$$V_v(t) = -M\ddot{q}_B(t) \tag{27}$$

$$V_p(t) = \begin{cases} 0 \text{when } q(t) \geq -D_0 \\ -C_p\dot{q}(t) - K_p q(t) \text{when } q(t) < -D_0 \end{cases} \tag{28}$$

where $\ddot{q}_B(t)$ is the second-order time derivative of the charge from the pseudo-voltage source $V_v(t)$.

With the mechanical model's equivalent circuit components identified, the next step is to transform the electrical model into the corresponding ECM. The electrical governing equation for a single tribo-cell ($N = 1$), as given in Eq. (19), can be rearranged into the following form:

$$R\frac{dQ(t)}{dt} = V_{oc}(t) - V_{ic}(t) = \frac{mn\alpha d_G(t)\sigma A_c}{WH\varepsilon_0} - \frac{Q(t)[A_c\varepsilon_r mn\alpha d_G(t) + hWH]}{A_c\varepsilon_0\varepsilon_r WH} \tag{29}$$

The right-hand side of Eq. (29) consists of two terms: the open-circuit voltage V_{oc}, arising from the separation of polarized charges on the triboelectric contact surfaces, and the capacitance term V_{ic}, which results from the inherent capacitance between the two electrodes [47]. These terms are defined as

$$V_{oc} = \frac{mn\alpha d_G(t)\sigma A_c}{WH\varepsilon_0} \tag{30}$$

$$V_{ic} = \frac{Q(t)[A_c\varepsilon_r mn\alpha d_G(t) + hWH]}{A_c\varepsilon_0\varepsilon_r WH} \tag{31}$$

where $d_G(t)$ is given by

$$d_G(t) = d_0 + \frac{2}{a-1}q(t) \tag{32}$$

With all the equivalent circuit components identified, the ECM for the BOTEH is implemented in the circuit simulation software Simetrix, as shown in Fig. 15. In the mechanical part, V_v, V_p, L_{eq}, C_{eq}, and R_{eq} are connected in series, with V_p acting as an arbitrarily defined voltage source. This source has two input electrodes, in_a and in_b, which probe the voltage V_{eq} across C_{eq}, as V_p requires V_{eq} to compute $q(t)$, an input

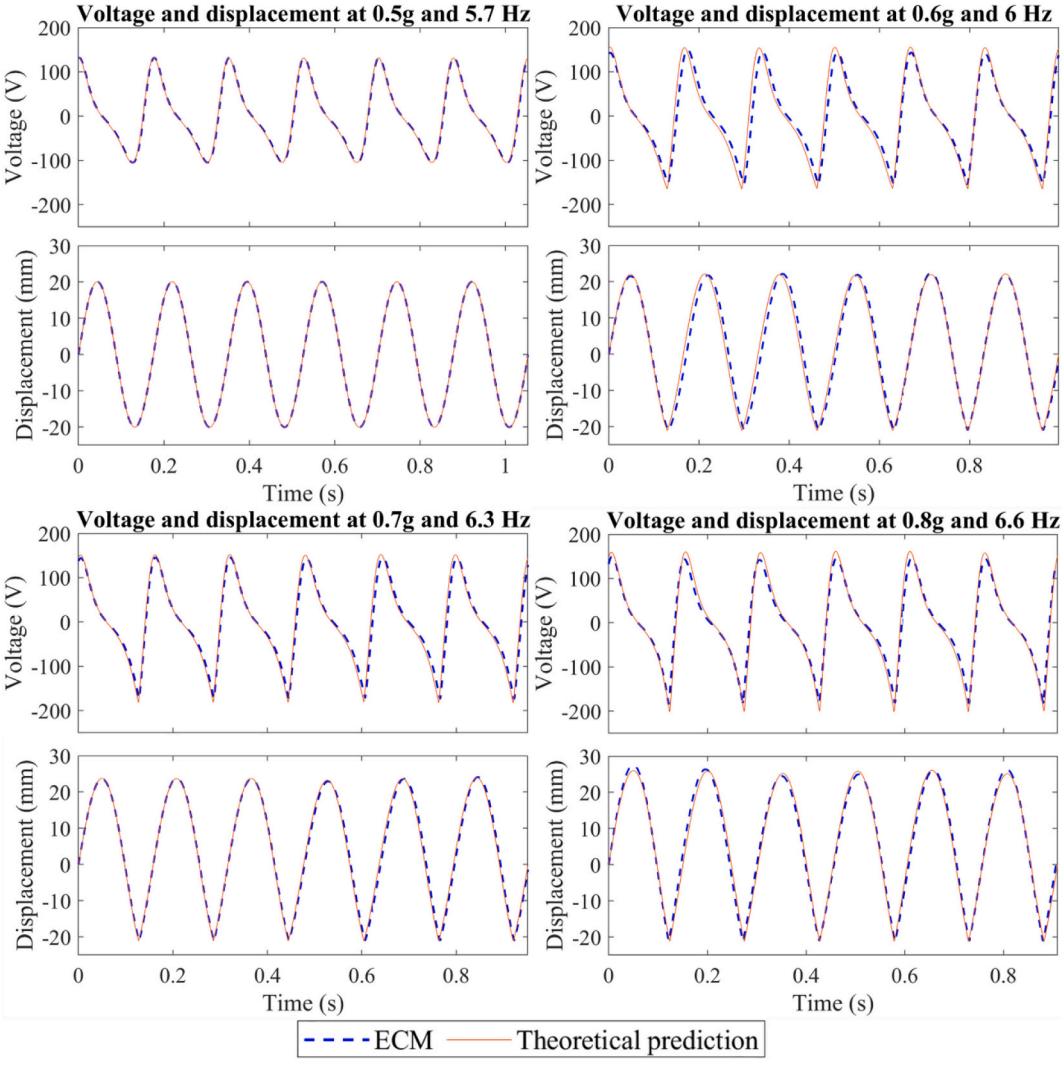

Fig. 16. Time-domain voltage and displacement responses of BOTEH from ECM simulation and theoretical predication.

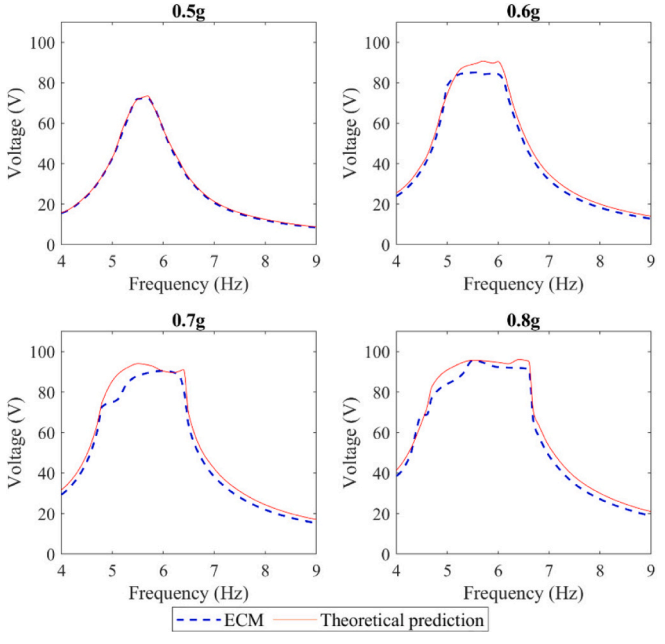

(a)

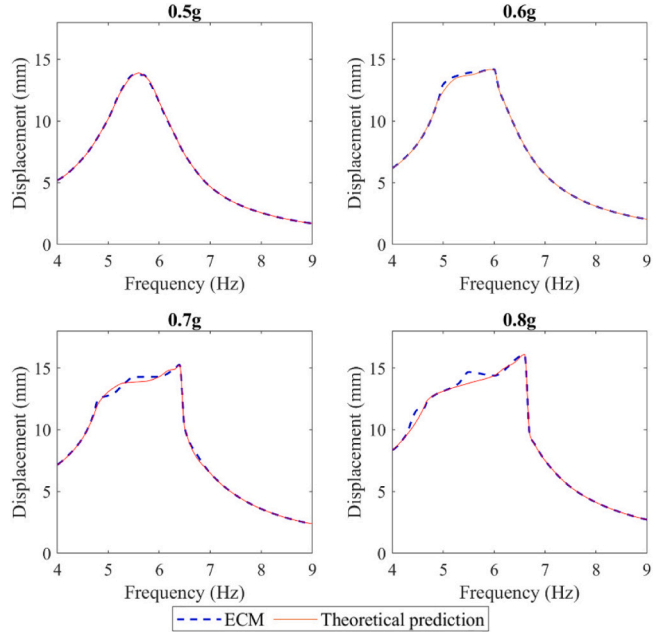

(b)

Fig. 17. ECM simulation and theoretical predication of (a) RMS voltage response and (b) RMS displacement response of BOTEH in frequency domain.

variable of V_p according to Eq. (28). The pseudo-charge $q(t)$ is computed using the expression

$$q(t) = \frac{V_{eq}}{C_{eq}} \tag{33}$$

In the electrical part, the model consists of V_{oc}, V_{ic}, and R in series. However, extracting the transferred charge $Q(t)$ directly from this part is not straightforward. To address this, a pseudo-capacitor C_{ic} is added, connected to a pseudo-current source I_c, which outputs the same current $I(t)$ flowing through the electrical circuit. By probing the voltage V_c across C_{ic}, the transferred charge $Q(t)$ can be determined as

$$Q(t) = \int_0^t I(\tau)d\tau = C_{ic}V_c(t) \tag{34}$$

Here, V_{oc} has two input electrodes probing V_{eq} to compute $q(t)$, while V_{ic} has two electrode pairs probing both V_{eq} across C_{eq} and V_c across C_{ic}, as both $q(t)$ and $Q(t)$ are programmed as input variables. Finally, with Probe-V_{eq} recording the voltage V_{eq} and Probe-R measuring the BOTEH's output voltage across R, the ECM-simulated electromechanical responses of the BOTEH can be generated.

First, the time-domain electromechanical responses are analyzed when the BOTEH experiences the highest charge transfer at excitation accelerations from 0.5 g to 0.8 g in increments of 0.1 g, as shown in Fig. 16. The results demonstrate a strong agreement between the ECM simulation and theoretical prediction of time-domain responses, though minor discrepancies emerge at higher excitation levels due to slight numerical instabilities. These discrepancies arise because the circuit simulation software employs a different numerical solver than MATLAB's ODE23TB. Nevertheless, the overall agreement between the ECM and theoretical results remains remarkably high.

Following the time-domain analysis, the ECM simulation and theoretical prediction of frequency-domain responses are compared in Fig. 17, which presents the root mean square (RMS) voltage and displacement responses of the BOTEH. Fig. 17 confirms that the ECM effectively captures the electromechanical dynamics predicted by the numerical solver. However, minor numerical instabilities at higher excitation levels lead to small discrepancies.

4.4. *Performance showcase of BOTEH*

In Subsection 4.2, with the external resistance $R = 100$ MΩ, it can be seen that the maximum RMS voltage output of the BOTEH can reach up to 102.8 V at a 6.6 Hz forcing frequency and 0.8 g excitation acceleration. The BOTEH's time-domain peak-to-peak voltage at this point can be as much as 355.7 V. These values reveal that the BOTEH proposed in this study has outstanding performance. To provide more illustrations of the BOTEH's performance, further experiments were conducted. A straightforward and graphical way to illustrate the BOTEH's performance is to characterize its LED illumination capability. The BOTEH's electrodes were connected to the AC ports of a bridge rectifier, whose DC ports were connected to 24 LEDs in series according to the scheme shown in Fig. 18 (a). An excitation level of 0.8 g and a forcing frequency of 6.6 Hz were supplied to the BOTEH, which then brightly illuminated the 24 LEDs as shown in Fig. 18 (b) that shows the illuminated LEDs forming the pattern of "NTU" in darkness.

A more practical application is powering an actual IoT device. The device chosen for demonstration in this study is a vibration-powered sensing node (ViPSN) [48], an Internet-of-Things sensing platform that is programmable and can host different replaceable modules on a motherboard. The ViPSN used in this study consists of an energy enhancement unit (EEU), an energy management unit (EMU), and an energy user unit (EUU). The EEU is essentially a bridge rectifier that converts the AC voltage response from the BOTEH into full-wave DC output. The EMU module includes a 47 μF capacitor. Once the capacitor on the EMU is charged to a threshold of 5 V, the EMU releases a certain amount of energy to power and trigger the operation of the EUU. The EUU module used in this study is a temperature-sensing node that measures the ambient temperature and transmits the data to a mobile application *via* Bluetooth. The BOTEH's electrodes are connected to the AC ports of the bridge rectifier on the EEU, as shown in Fig. 19 (a), and vibration with 0.8 g excitation and 6.6 Hz forcing frequency is applied to the BOTEH. Fig. 19 (a) also provides a detailed illustration of the different modules on the ViPSN. The BOTEH then starts charging the 47 μF capacitor on the EMU under the forcing vibration until the capacitor reaches 5 V, which takes around 2.17 min, as illustrated in Fig. 19 (b). A

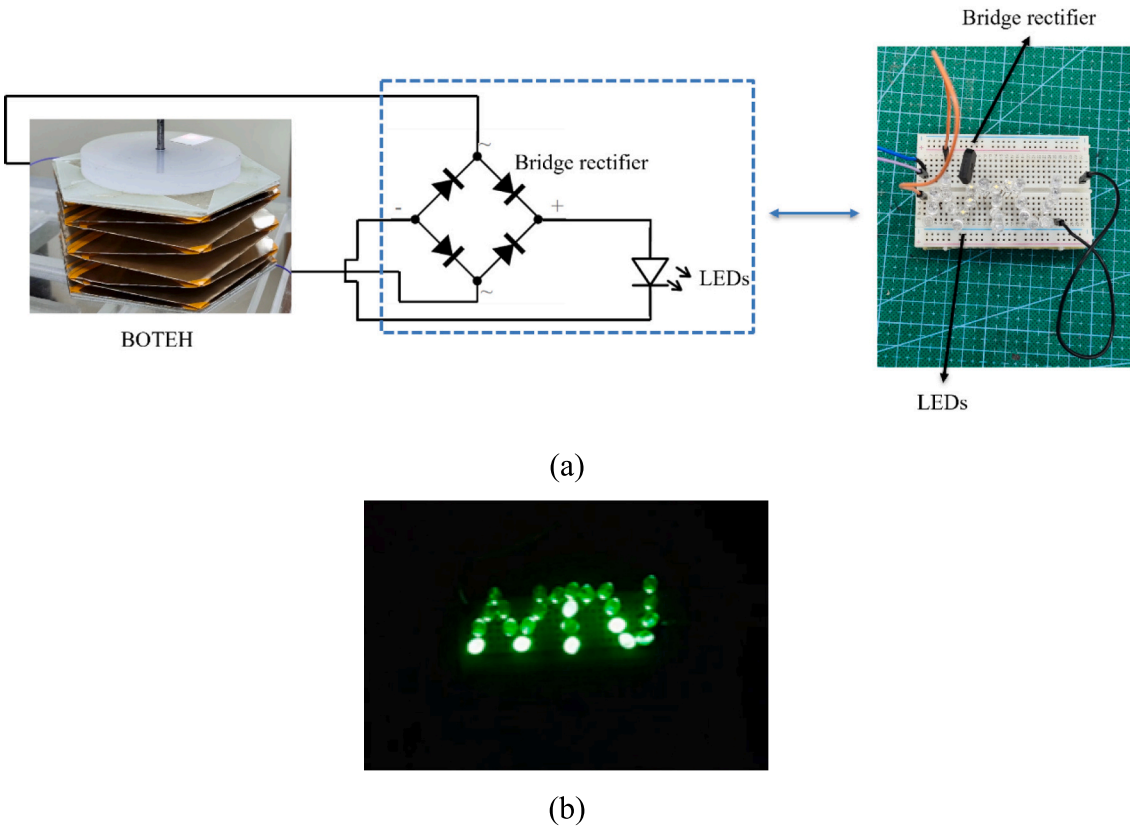

Fig. 18. (a) Setup of the LED illumination experiment and (b) instantaneous illumination effect of 24 LEDs in series forming the pattern of "NTU".

video demonstration of the charging process under the shaker's excitation can be found in Supplementary material S1. In the video, it can be seen that the temperature sensor is then triggered and sends the temperature measurement to the mobile app, which shows the location of the sensor and the measured ambient temperature value, as shown in Fig. 19 (a). As an additional demonstration, the BOTEH was tapped on the mass block's top by hand at around an 8 Hz tapping frequency to charge the capacitor on the EEU. The video demonstration of the hand-tapping experiment can be found in Supplementary material S2. The hand-tapped charging curve is shown in Fig. 19 (c), where the trigger point occurs after around 40 s, which is considerably shorter than the duration under the shaker's excitation. Note that the time it takes the BOTEH to trigger the ViPSN's operation in the video is different because the video was taken separately from the experimental results shown in Fig. 19 (c). The reason for the quicker charging from hand tapping compared to shaker excitation is that the triboelectric contact surfaces experience more complete contact-separation cycles when tapped. This shows that intensive human motion can result in the BOTEH producing a large amount of electrical energy.

The qualitative demonstrations above indicate that the BOTEH used in this study has strong potential for harvesting kinetic energy from low-frequency ambient vibrations (< 9 Hz) and human motion. One example of low-frequency ambient vibration is ocean waves, which typically consist of random vibrations with mixed amplitudes and frequencies below 9 Hz, as demonstrated by Tao et al. [32]. In their study, the OTEH lacked axial elasticity, requiring four identical OTEHs to harvest ocean-wave energy through transverse elasticity. In contrast, the BOTEH in this study features axial elasticity, which could reduce space requirements in practical ocean-wave energy harvesting applications. Moreover, its axial elasticity can be easily tuned by adjusting the proof mass M or modifying the geometric configuration of the origami structure.

For human-motion energy harvesting, researchers have designed TEHs to capitalize on natural human movement. For instance, as a person walks, their shoe soles repeatedly press against the ground, creating an opportunity to embed a TEH within the sole to generate electricity through repeated compression. A notable example is the stacked TEH developed by Zhu et al. [49]. Due to its stacked and flexible nature, the BOTEH in this study can also be adapted for this purpose by optimizing its geometric parameters. Additionally, its axial elasticity offers a potential advantage over conventional stacked TEHs—when the shoe sole lifts off the ground, the BOTEH can naturally spring back, preparing for the next press-release cycle, thereby enhancing energy conversion efficiency.

Aside from the qualitative demonstration of the BOTEH's performance discussed above, quantitative characterizations of the performance were also conducted, including determining the optimal output power of the BOTEH. To experimentally determine the optimal power of the BOTEH, the LEDs connected to the DC output ports in Fig. 18 (a) were replaced with a filtering capacitor C_f and a variable external resistor R in parallel, as illustrated by the scheme in Fig. 20 (a). An electrometer was used to record the DC voltage across the capacitor C_f. When the voltage across C_f reached its maximum V_{max}, the output power

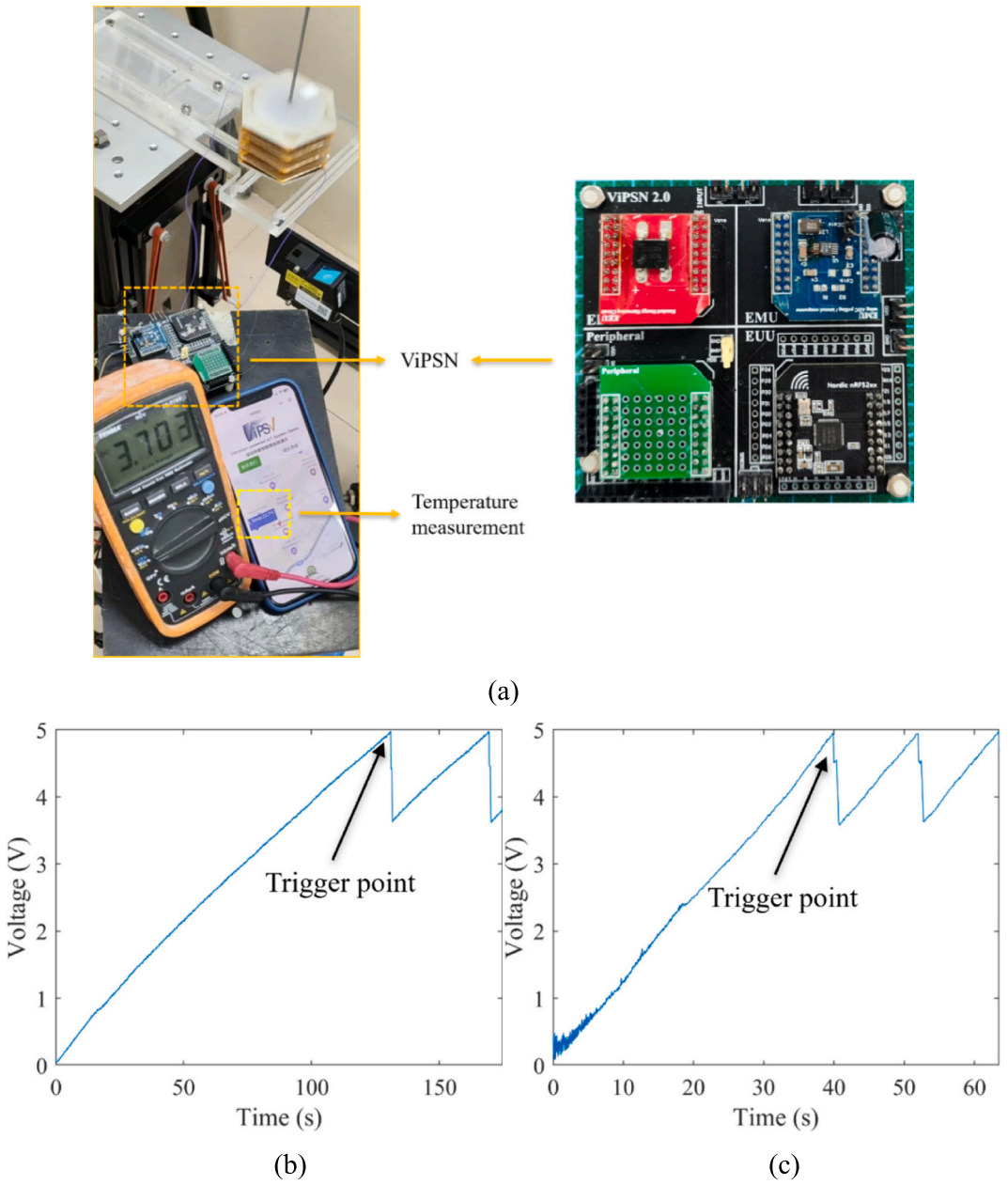

Fig. 19. (a) Setup of ViPSN powering experiment when BOTEH is under seismic shaker's excitation, (b) charging curve of capacitor on EEU when BOTEH is excited by shaker, and (c) charging curve of capacitor on EEU when BOTEH is continuously tapped by hand.

P at the specific R was then $\frac{V_{\max}^2}{R}$. For example, Fig. 20 (b) shows the charging curve of $C_f = 100$ nF with $R = 80$ MΩ. In this case, the maximum possible DC voltage accumulated in C_f reaches up to 97.6 V, resulting in an output power of 119 μW. Because of the high internal impedance of TEHs [50], it is necessary to adjust R until the maximum power P occurs. Fig. 20 (c) shows the BOTEH's output power against R at 0.8 g excitation and 6.6 Hz forcing frequency. It can be seen that the optimal power $P = 119$ μW occurs at around $R = 80$ MΩ.

As an additional quantitative performance demonstration, a capacitor charging test was conducted after the resistor R in Fig. 20 (a) was removed. The forcing frequency was kept at 6.6 Hz with 0.8 g excitation, and the BOTEH charged the capacitor C_f with varied capacitances from 1 μF to 5 μF in 1 μF increments for 60 s each. After that, the capacitor C_f was kept at 3 μF, and the excitation level was varied from 0.5 g to 0.8 g in 0.1 g increments, with the forcing frequencies adjusted to match the shifted natural frequency of the BOTEH at each excitation level. The results are shown in Fig. 21. It can be seen that, at 0.8 g excitation, the BOTEH can at least charge a 5 μF capacitor to more than 20 V in one minute and charge a 3 μF capacitor to over 20 V when given 0.5 g excitation.

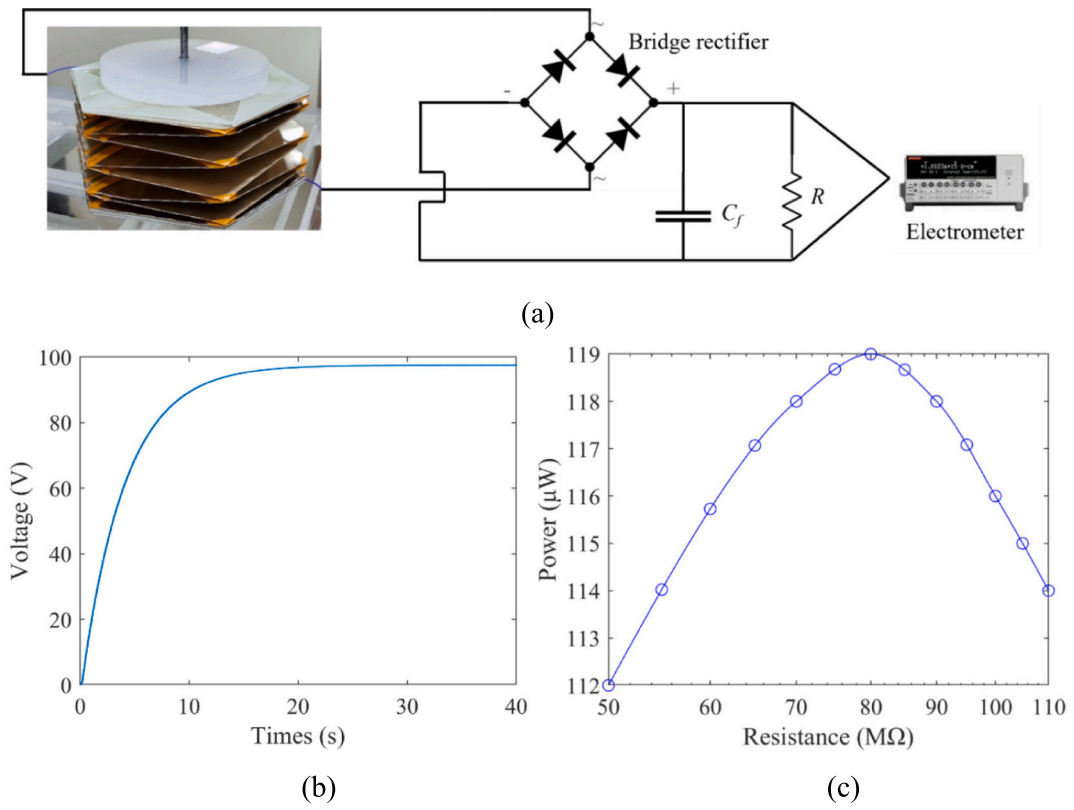

Fig. 20. (a) Illustration of experimental setup for BOTEH's optimal power determination; (b) charging curve of a 100 nF capacitor with $R = 80$ MΩ and (c) BOTEH's output power against external resistance under 0.8 g excitation and 6.6 Hz forcing frequency.

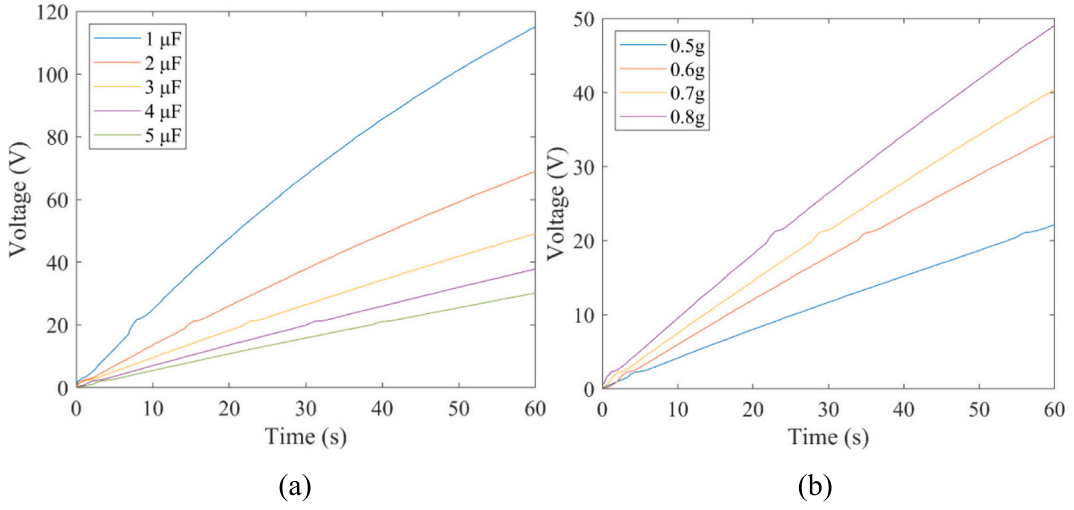

Fig. 21. (a) Sharging curves of different capacitors with 0.8 g excitation and 6.6 Hz forcing frequency, and (b) charging curves of 3 μF capacitor with different excitation levels.

5. Conclusion

This study successfully established and experimentally validated a novel electromechanical model for an elastic origami-structured triboelectric vibration energy harvester (OTEH). The detailed operating mechanisms of an elastic OTEH were thoroughly explored, leading to the derivation of a comprehensive model that couples electrical and mechanical components. The design and fabrication processes for a bellow-origami structured OTEH (BOTEH), which served as the basis for experimental validation, were also meticulously outlined. Preliminary experiments were conducted to determine key parameters for the model, which were subsequently used in simulations. The numerical simulation results for the BOTEH's time-domain and frequency-domain electromechanical responses under base vibration were validated experimentally, demonstrating the model's high accuracy in predicting the dynamic behavior of the BOTEH during vibration energy harvesting. For further validation, the equivalent circuit model (ECM) of the BOTEH's electromechanical system was established and used to verify the numerical simulation results. Additional experiments highlighted the BOTEH's capability to illuminate LEDs and activate an IoT sensing node when powered by base vibration. The key conclusions of this study are as follows.

- This study presents, for the first time, a novel and comprehensive electromechanical model for an elastic OTEH designed for vibration energy harvesting. The model offers new insights into simplifying mechanical models of OTEHs while accurately predicting their electromechanical responses under base vibration, eliminating the need for trial-and-error adjustments.
- The model introduces a new electrical framework based on a capacitive model for non-parallel triangular plates, addressing the triangular contact surfaces commonly found in many elastic OTEHs.
- Unlike previous studies that primarily focus on energy harvesting from press-and-release motions, this study pioneers the modeling and experimental validation of an OTEH specifically for vibration energy harvesting. It demonstrates how the enlarged contact area from stacked origami structures can be effectively utilized in triboelectric vibration energy harvesting. To our knowledge, no prior research has addressed the modeling and validation of an OTEH's electromechanical behavior under base vibration.
- The proposed electromechanical model, validated through experiments and an alternative modeling technique, the ECM, has shown high accuracy in predicting the nonlinear time-domain and frequency-domain dynamics of the BOTEH. Additionally, the model's incorporation of geometric parameters allows it to be generalized for other similarly structured elastic OTEHs with various cross-sections and dimensions, making it a valuable tool for the design and parameter optimization of elastic OTEHs for vibration energy harvesting.
- The BOTEH demonstrated significant practical utility by illuminating 24 LEDs and activating an IoT vibration-powered sensing node (ViPSN) when powered by base vibration. It triggered the sensor's first operation in approximately 2.17 min under 0.8 g excitation and 6.6 Hz forcing frequency, and in about 40 s under hand-tapping conditions. Quantitative characterization revealed that, under 0.8 g excitation and 100 MΩ external resistance, the BOTEH achieved a peak-to-peak voltage of up to 355.7 V in the time domain and an RMS voltage of up to 102.8 V in the frequency domain, with an optimal output power of 119 μW at 80 MΩ resistance.

Supplementary data to this article can be found online at https://doi.org/10.1016/j.apenergy.2025.125761.

CRediT authorship contribution statement

Zicheng Liu: Writing – original draft, Visualization, Validation, Software, Methodology, Formal analysis, Data curation, Conceptualization. **Guobiao Hu:** Writing – review & editing, Resources, Investigation, Conceptualization. **Yawei Wang:** Writing – review & editing, Resources, Methodology, Investigation. **Heesoo Yoon:** Resources, Methodology, Investigation. **Chaoyang Zhao:** Writing – review & editing, Software, Resources. **Xin Li:** Resources. **Yaowen Yang:** Writing – review & editing, Supervision, Resources, Project administration, Investigation, Conceptualization.

Declaration of competing interest

The authors declare that they have no known competing financial interests or personal relationships that could have appeared to influence the work reported in this paper.

Data availability

Data will be made available on request.

References

[1] Sanislav T, Mois GD, Zeadally S, Folea SC. Energy harvesting techniques for internet of things (IoT). IEEE Access 2021;9:39530–49.
[2] Zeadally S, Shaikh FK, Talpur A, Sheng QZ. Design architectures for energy harvesting in the internet of things. Renew Sust Energ Rev 2020;128:109901.
[3] Zuo L, Scully B, Shestani J, Zhou Y. Design and characterization of an electromagnetic energy harvester for vehicle suspensions. Smart Mater Struct 2010;19(4):045003.
[4] Miao G, Fang S, Wang S, Zhou S. A low-frequency rotational electromagnetic energy harvester using a magnetic plucking mechanism. Appl Energy 2022;305:117838.
[5] Zhang L, Zhang F, Qin Z, Han Q, Wang T, Chu F. Piezoelectric energy harvester for rolling bearings with capability of self-powered condition monitoring. Energy 2022;238:121770.
[6] He L, Zhou J, Zhang Z, Gu X, Yu Y, Cheng G. Research on multi-group dual piezoelectric energy harvester driven by inertial wheel with magnet coupling and plucking. Energy Convers Manag 2021;243:114351.
[7] Lensvelt R, Fey RH, Mestrom R, Nijmeijer H. Design and numerical analysis of an electrostatic energy harvester with impact for frequency up-conversion. J Comput Nonlinear Dyn 2020;15(5):051005.
[8] Vysotskyi B, Campos J-FA, Lefeuvre E, Brenes A. Dynamic analysis of a novel two-sided nonlinear MEMS electrostatic energy harvester. Mechanical Syst Sig Processing 2024;206:110932.
[9] Hu S, et al. Vibration-driven triboelectric nanogenerator for vibration attenuation and condition monitoring for transmission lines. Nano Lett 2022;22(13):5584–91.
[10] Yang W, et al. Harvesting vibration energy by a triple-cantilever based triboelectric nanogenerator. Nano Res 2013;6:880–6.
[11] Yang J, et al. Broadband vibrational energy harvesting based on a triboelectric nanogenerator. Adv Energy Mater 2014;4(6):1301322.
[12] Li Y, et al. Low-cost, environmentally friendly, and high-performance triboelectric nanogenerator based on a common waste material. ACS Appl Mater Interfaces 2021;13(26):30776–84.
[13] Lv S, Zhang X, Huang T, Yu H, Zhu M. Interconnected array design for enhancing the performance of an enclosed flexible triboelectric nanogenerator. Nano Energy 2021;89:106476.
[14] Li X, et al. A highly efficient constant-voltage triboelectric nanogenerator. Energy Environ Sci 2022;15(3):1334–45.
[15] Zhou L, Liu D, Wang J, Wang ZL. Triboelectric nanogenerators: fundamental physics and potential applications. Friction 2020;8:481–506.
[16] Wang ZL, et al. Triboelectric nanogenerator: vertical contact-separation mode. Triboelectric nanogenerators 2016:23–47.
[17] Wang ZL, et al. Triboelectric nanogenerator: lateral sliding mode. Triboelectric nanogenerators 2016:49–90.
[18] Wang ZL, et al. Triboelectric nanogenerator: freestanding triboelectric-layer mode. Triboelectric Nanogenerators 2016:109–53.
[19] Li Z, et al. On the performance of freestanding rolling mode triboelectric nanogenerators from rotational excitations for smart tires. Nano Energy 2023;113:108595.
[20] Wang ZL, et al. Triboelectric nanogenerator: single-electrode mode. Springer; 2016.
[21] Yang W, et al. 3D stack integrated triboelectric nanogenerator for harvesting vibration energy. Adv Funct Mater 2014;24(26):4090–6.
[22] Liu G, Guo H, Chen L, Wang X, Wei D, Hu C. Double-induced-mode integrated triboelectric nanogenerator based on spring steel to maximize space utilization. Nano Res 2016;9:3355–63.
[23] Li Y, et al. Multi-layered triboelectric nanogenerator incorporated with self-charge excitation for efficient water wave energy harvesting. Appl Energy 2023;336:120792.
[24] Sargent B, et al. An origami-based medical support system to mitigate flexible shaft buckling. J Mech Robot 2020;12(4):041005.
[25] Suzuki H, Wood RJ. Origami-inspired miniature manipulator for teleoperated microsurgery. Nat Machine Intelligence 2020;2(8):437–46.
[26] Lee J-Y, et al. Development of a multi-functional soft robot (SNUMAX) and performance in RoboSoft grand challenge. Front Robotics AI 2016;3:63.
[27] Zhakypov Z, Paik J. Design methodology for constructing multimaterial origami robots and machines. IEEE Trans Robotics 2018;34(1):151–65.
[28] Chen T, Bilal OR, Lang R, Daraio C, Shea K. Autonomous deployment of a solar panel using elastic origami and distributed shape-memory-polymer actuators. Phys Rev Appl 2019;11(6):064069.
[29] Zirbel SA, Trease BP, Thomson MW, Lang RJ, Magleby SP, Howell LH. Hanaflex: a large solar array for space applications. In: Micro-and Nanotechnology Sensors, Systems, and Applications VII. 9467. SPIE; 2015. p. 179–87.
[30] Chung J, et al. Triangulated cylinder origami-based piezoelectric/triboelectric hybrid generator to harvest coupled axial and rotational motion. Research 2021;2021:7248579.
[31] Hu G, Zhao C, Yang Y, Li X, Liang J. Triboelectric energy harvesting using an origami-inspired structure. Appl Energy 2022;306:118037.
[32] Tao K, et al. Origami-inspired electret-based triboelectric generator for biomechanical and ocean wave energy harvesting. Nano Energy 2020;67:104197.
[33] Tao K, et al. Miura-origami-inspired electret/triboelectric power generator for wearable energy harvesting with water-proof capability. Microsyst & Nanoeng 2020;6(1):56.
[34] Chung S-H, et al. Enhancing strategy of triboelectric Nanogenerator via origami pattern by harvesting mechanical motion and wind flow. Int J Energy Res 2024;2024(1):2120442.

[35] Zhang H, et al. Origami-tessellation-based triboelectric nanogenerator for energy harvesting with application in road pavement. Nano Energy 2020;78:105177.
[36] Jiang T, Yao Y, Xu L, Zhang L, Xiao T, Wang ZL. Spring-assisted triboelectric nanogenerator for efficiently harvesting water wave energy. Nano Energy 2017;31:560–7.
[37] Zhao C, Yang Y, Upadrashta D, Zhao L. Design, modeling and experimental validation of a low-frequency cantilever triboelectric energy harvester. Energy 2021;214:118885.
[38] Zhao C, Hu G, Li X, Liu Z, Yuan W, Yang Y. Wide-bandwidth triboelectric energy harvester combining impact nonlinearity and multi-resonance method. Appl Energy 2023;348:121530.
[39] Fu Y, Ouyang H, Benjamin Davis R. Nonlinear structural dynamics of a new sliding-mode triboelectric energy harvester with multistability. Nonlinear Dyn 2020;100:1941–62.
[40] Fu Y, Ouyang H, Davis RB. Effects of electrical properties on vibrations via electromechanical coupling in triboelectric energy harvesting. J Phys D Appl Phys 2020;53(21):215501.
[41] Zhu D, Tudor MJ, Beeby SP. Strategies for increasing the operating frequency range of vibration energy harvesters: a review. Meas Sci Technol 2009;21(2):022001.
[42] Mann B, Sims N. Energy harvesting from the nonlinear oscillations of magnetic levitation. J Sound Vib 2009;319(1–2):515–30.
[43] Zhang X, Zhang W, Lei G. A review of li-ion battery equivalent circuit models. Trans Electr Electron Mater 2016;17(6):311–6.
[44] Elvin NG, Elvin AA. A general equivalent circuit model for piezoelectric generators. J Intell Mater Syst Struct 2009;20(1):3–9.
[45] Jia J, Shan X, Zhang X, Xie T, Yang Y. Equivalent circuit modeling and analysis of aerodynamic vortex-induced piezoelectric energy harvesting. Smart Mater Struct 2022;31(3):035009.
[46] Bayik B, Aghakhani A, Basdogan I, Erturk A. Equivalent circuit modeling of a piezo-patch energy harvester on a thin plate with AC–DC conversion. Smart Mater Struct 2016;25(5):055015.
[47] Niu S, Wang ZL. Theoretical systems of triboelectric nanogenerators. Nano Energy 2015;14:161–92.
[48] Li X, et al. ViPSN: a vibration-powered IoT platform. IEEE Internet Things J 2020;8(3):1728–39.
[49] Zhu G, Bai P, Chen J, Wang ZL. Power-generating shoe insole based on triboelectric nanogenerators for self-powered consumer electronics. Nano Energy 2013;2(5):688–92.
[50] Rasel MS, et al. An impedance tunable and highly efficient triboelectric nanogenerator for large-scale, ultra-sensitive pressure sensing applications. Nano Energy 2018;49:603–13.